Bioactive Materials 41 (2024) 174–192

Contents lists available at ScienceDirect

Bioactive Materials

journal homepage: www.keaipublishing.com/en/journals/bioactive-materials

Protonated-chitosan sponge with procoagulation activity for hemostasis in coagulopathy

Zhenhua Huang [a], Dong Zhang [a], Laiqiang Tong [a], Fan Gao [a], Shaozan Zhang [a], Xinqing Wang [a], Yina Xie [a], Fangping Chen [a,b,*], Changsheng Liu [a,b,**]

[a] Engineering Research Center for Biomedical Materials of Ministry of Education, East China University of Science and Technology, Shanghai, 200237, PR China
[b] Key Laboratory for Ultrafine Materials of Ministry of Education, School of Materials Science and Engineering, East China University of Science and Technology, Shanghai, 200237, PR China

A B S T R A C T

Hemostatic materials are essential for managing acute bleeding in medical settings. Chitosan (CS) shows promise in hemostasis but its underlying mechanism remains incompletely understood. We unexpectedly discovered that certain protonated-chitosan (PCS) rapidly assembled plasma proteins to form protein membrane (PM) upon contact with platelet-poor plasma (PPP). We hypothesized that the novel observation was intricately related to the procoagulant effect of chitosan. Herein, the study aimed to elucidate the conditions necessary and mechanism for PM formation, identify the proteins within the PM and PCS's procoagulant action at the molecule levels. We confirmed that the amount of $-NH_3^+$ groups (>4.9 mmol/g) on PCS molecules played a crucial role in promoting coagulation. The $-NH_3^+$ group interacted with blood's multiple active components to exert hemostatic effects: assembling plasma proteins including coagulation factors such as FII, FV, FX, activating blood cells and promoting the secretion of coagulation-related substances (FV, ADP, etc) by platelets. Notably, the hemostatic mechanism can be extended to protonated-chitosan derivatives like quaternized, alkylated, and catechol-chitosan. In the blood clotting index (BCI) experiment, compared to other groups, PCS95 achieved the lowest BCI value (~6 %) within 30 s. Protonated-chitosan exhibited excellent biocompatibility and antibacterial properties, with PCS95 demonstrating inhibition effectiveness of over 95 % against *Escherichia coli* (*E.coil*) and *Staphylococcus aureus* (*S. aureus*). Moreover, PCS performed enhanced hemostatic effectiveness over chitosan-based commercially agents (Celox™ and ChitoGauze®XR) in diverse bleeding models. In particular, PCS95 reduced bleeding time by 70 % in rabbit models of coagulopathy. Overall, this study investigated the coagulation mechanism of materials at the molecular level, paving the way for innovative approaches in designing new hemostatic materials.

1. Introduction

Excessive blood loss is a leading cause of mortality in various settings including military conflicts, traffic accidents, and surgical operations. Rapid and effective hemostasis are essential for preventing massive bleeding, particularly for patients with coagulation disorders [1–3]. Despite significant progress in the field of hemostatic materials in recent decades, innovation has been impeded by the dependence on single hemostatic mechanisms and intricate fabrication processes. To enhance hemostatic efficacy, it is often required to embed hemostatic drugs such as thrombin [4,5] and tranexamic acid [6–8] into materials. However, the application of these coagulant drugs exacerbates the economic burden on patients and poses the potential risk of systemic thrombosis. Additionally, the emergence of numerous novel material fabrication techniques such as electrospinning [9,10], 3D printing [11], and ice template [12], the complexity of the production processes and substantial energy consumption have become significant limiting factors. Consequently, the ideal hemostatic material should inherently facilitate coagulation, be easily prepared, and be cost-effective.

Chitosan, a positively charged natural polymer, known for its wide-ranging applications in hemostasis [13–16], antibacterial [17,18], tissue engineering [19–21] and other fields [22,23]. Since William G. Malette discovered in 1983 that chitosan performed effective hemostatic effect, chitosan-based hemostatic materials have attracted considerable attention from researchers [24]. A number of commercial chitosan-based hemostatic products such as Celox™, HemCon®Bandage, AX-Surgi™ and others have been successively approved by FDA and widely used by military personnel, first responders, and emergency medical

Peer review under responsibility of KeAi Communications Co., Ltd.

* Corresponding author. Engineering Research Center for Biomedical Materials of Ministry of Education, East China University of Science and Technology, Shanghai, 200237, PR China.

** Corresponding author. Engineering Research Center for Biomedical Materials of Ministry of Education, East China University of Science and Technology, Shanghai, 200237, PR China.

E-mail addresses: huangzhenhua013@163.com (Z. Huang), fpchen@ecust.edu.cn (F. Chen), liucs@ecust.edu.cn (C. Liu).

https://doi.org/10.1016/j.bioactmat.2024.07.012
Received 21 April 2024; Received in revised form 20 June 2024; Accepted 7 July 2024

professionals worldwide. Recent advancements have further diversified the applications of chitosan and its derivatives, resulting in innovative hemostatic materials such as alkylated chitosan(AQS) [10,18,19], quaternary ammonium chitosan (QCS) [13], and chitosan-catechol(CHI–C) [3,24], which have proven effective in both standard and coagulopathically challenged bleeding scenarios.

Despite these advancements, the precise mechanisms through which chitosan exerts its hemostatic effects remain not fully understood. It is generally accepted that the positive charges on the $-NH_3^+$ groups in chitosan promote the adhesion and aggregation of erythrocytes and platelets [25]. Recent studies have demonstrated that chitosan can activate platelets via Toll-like receptor 2 (TLR2), facilitating hemostasis in individuals on oral antiplatelet medications [2]. The discovery changed the notion that chitosan didn't directly interact with physiological coagulation process. Interestingly, we unexpectedly discovered that certain chitosan solution rapidly formed protein membrane upon being dropped into plasma proteins solution, while this phenomenon was not observed with some other chitosan. This discovery prompted us to investigate the interaction between chitosan and blood. We hypothesized that the phenomenon was associated with the unique positive charge effect of chitosan molecules. During the deacetylation process, chitosan possesses a weak positive charge, and under acidic condition, the amino groups are protonated ($-NH_2 \rightarrow -NH_3^+$), further enhancing its charge-carrying capacity.

To this end, we initially synthesized three protonated-chitosan with varying degrees of deacetylation (PCS95, PCS80, PCS65). These were subsequently processed into protonated-chitosan sponges using a simple freeze-drying technique. We explored the interaction between protonated-chitosan and plasma proteins, as well as blood cells, using techniques such as proteomics, isothermal titration calorimetry, and flow cytometry, etc. Our research results indicated that protonated-chitosan with a high degree of deacetylation (HDPCS) demonstrated superior procoagulant properties. The hemostatic mechanism of HDPCS was primarily reflected in its ability to recruit coagulation factors present in the blood and to assemble plasma proteins. It activated, adhered, and aggregated platelets, subsequently promoting the secretion of intracellular hemostatic substances within the platelets. The activated platelets provided active sites for the assembly of coagulation factors, leading to the generation of thrombin and ultimately facilitating the formation of blood clots (Scheme 1). Additionally, due to its unique coagulation-promoting effects, PCS95 demonstrated exceptional hemostatic performance in a rabbit coagulopathy bleeding model. Our work not only provides novel insights into the hemostatic mechanism of chitosan-based hemostatic materials, but also paves the way for the development of a new generation of active hemostatic agents.

2. Experimental section

2.1. Materials

Chitosan (viscosity, 100–200 mPa·s; 95 % deacetylated) and 1-(3-Dimethylaminopropyl)-3-ethylcarbodiimide hydrochloride (EDC·HCl,

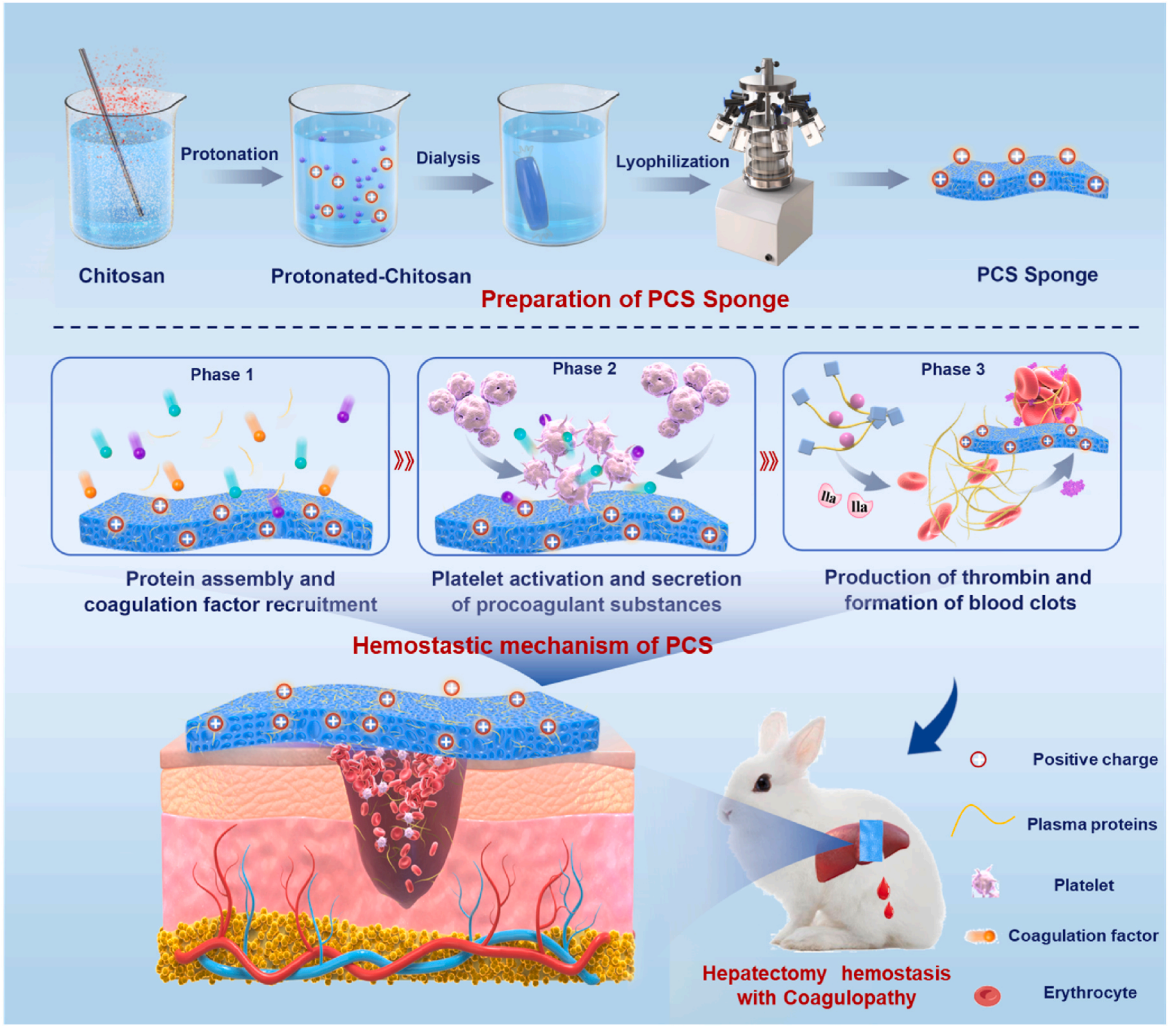

Scheme 1. The schematic diagram of the preparation and hemostatic mechanism of PCS sponge and its application in hemostasis.

purity 98 %) were purchased from Shanghai Aladdin Bio-Chem Technology Co., LTD (China). Acetic acid (99 %+, extra pure) was sourced from Sinopharm Chemical Reagents Co., Ltd (China). Animals were supplied by Shanghai Jiesijie Experimental Animal Co., Ltd.

2.2. Preparation of PCS95, PCS80 and PCS65

The protonated-chitosan (PCS) was prepared by treating chitosan with acidic solution. Briefly, 1g chitosan (viscosity, 100–200 mPa·s; 95 % deacetylated) was dissolved in HCl solution (100 mL, 0.1 M). The pH of chitosan solution was adjusted to 4.0 with $NaHCO_3$ (1 M). PCS95 was then prepared by freeze-drying after 3 days of dialysis in deionized water.

PCS80 and PCS65 were prepared by coupling chitosan (viscosity 100–200 mPa·s, 95 % deacetylated) and acetic acid (HAc) with EDC·HCl. Briefly, 1 g chitosan was dissolved in HCl solution (100 mL, 0.1 M). Then, 5.9 mL of HAc (1 M) was added to solution, and the pH was adjusted to 4.8 with 1 M $NaHCO_3$. EDC·HCl (1.131 g, 5.9 mmol) was added into the solution and the mixture was reacted at 40 °C for 12 h. After the reaction, the pH was adjusted to 4.0 and the solution was transferred to a dialysis bag (molecular weight cut-off (MWCO), 14000) to remove free hydrogen ions and by-products, with water changes three times a day over 3 days. The dialyzed solution was then freeze-dried and stored under vacuum at room temperature for future use.

2.3. Characterization of PCS

The PCS sponges were compressed into sheets, and its absorption spectrum was recorded by ATR-FTIR (Nicolet 6700, Thermo Fisher Scientific, USA) with a scanning range of 4000-500 cm^{-1}.

To confirm the degree of deacetylation, the PCS sponges were dissolved in deuterated water (D_2O, 10 mg/mL) and were analysed by ^1H NMR (Ascend 600, Bruker, Germany). The deacetylation degree of protonated-chitosan was calculated using MNova 10.0.1 (Mestrelab Research, Spain) software.

Gel permeation chromatography (GPC, waters 1525, Waters Corporation, USA) was performed to analyze the molecular weight of PCS95, PCS80 and PCS65 solution. PCS was dissolved in ultrapure water at a concentration of 2 mg/mL, and the sample solution was filtered through a 0.45 μm filter membrane before analysis. 50 μL sample was injected into the system at a flow rate of 1 mL/min, using a Shodex SB-806 M chromatographic column. The column and detectors was maintained at a temperature of 40 °C. The molecular parameters were calculated with the Waters Breeze GPC software.

Rheological analysis of PCS was performed on a rheometer (MARS 3, Thermo Hakke, USA) at 25.0 °C, using a 20.0 mm parallel plate with plate gap of 0.1 mm. 200 μL PCS solution was dripped onto plate, and frequency sweeps were conducted at oscillation frequencies ranging from 0.1 to 10.0 Hz under a strain level of 5.0 %.

The charged properties of PCS were measured by a zeta potentiometer (Zetasizer Nano ZS90, Malvern, UK) and XPS (ESCALAB 250Xi, Thermo Fisher, USA). The sample was dissolved in deionized water at a concentration of 1 mg/mL, and the pH of the solution was adjusted to values between 2 and 7.4 using HCl (0.1 M) or NaOH (0.1 M). The zeta potential of the solution was measured using a zeta potentiometer and the measurement was repeated three times.

2.4. Separation of red blood cells (RBCs), platelets and plasma proteins

Anticoagulated whole blood from SD rats was centrifuged at 1800 rpm for 15 min, the pale yellow supernatant was collected to obtain platelet-rich plasma (PRP). The supernatant of PRP was further centrifuged at 1800 rpm to remove the residual erythrocytes to obtain pure PRP solution. The lower layer of blood was washed and centrifuged with PBS to obtain RBCs suspension. The PRP solution was then centrifuged at 3600 rpm for 10 min, and the supernatant was collected to yield platelet-poor plasma (PPP). The PPP solution was aspirated from the EP tube, and an equal volume of PBS was added to obtain a platelet suspension.

2.5. Formation of protein membrane

Protonated-chitosan (20 mg/mL) at various deacetylation degrees were added to PPP solution. Freeze and dry the resulting protein membrane, and the surface morphology of the protein membrane was observed with FESEM (S-4800, HITACHI, Japan).

2.6. Protein molecular weight analysis by SDS-PAGE

PCS95 was blended with PPP at a volume ratio of 3:1 to form protein membrane (PM) aggregates. PM were collected by centrifuging at 1000 rpm for 5 min, and an appropriate amount of deionized water was added for multiple centrifugal washes. 20 μL of protein solution was mixed with 80 μL of protein SDS-PAGE sample loading buffer (5 ×) and boiled for 10 min at 100 °C. This mixture was then loaded into the SDS-PAGE wells, alongside 10 μL of protein loading buffer and 10 μL of a protein marker (10–270 kDa) in each lane. The proteins and marker were separated using a 5–20 % polyacrylamide gel. The proteins in the gel were stained with Coomassie Brilliant Blue (BeyoBlue™, Beyotime Biotechnology, Shanghai, China) for 30 min, and photographs were taken.

2.7. LC-MS/MS

The protein components of PPP and PM were further analyzed by proteomics [26]. The protein samples were enzymolized and desalted to obtain the peptide samples. The samples were tested using LC-MS/MS in DIA mode. The MS (.raw) files obtained from the test was input into the DIA-NN (V.1.8.1) software for analysis. The detailed progress is available at supporting information.

2.8. Quantification of amino acids in PPP and PM

Amino acid components in PPP and PM were analyzed by amino acid analyzer (L-8900, Hitachi, Japan). Briefly, 20 mg sample and 50 mg phenol were dissolved in 10 mL of HCl solution (6 M). The mixture was cooled in an ice bath, then vacuumed and ventilated with nitrogen. Subsequently, the sample solution was hydrolyzed at 110 °C for 22 h, followed by cooling to room temperature. Finally, 5 mL of the filtrate was taken and diluted with water to a final volume of 50 mL. 1 mL of the resultant filtrate was extracted, dried using nitrogen gas, and redissolved in HCl (0.02 M) solution after drying. It was then filtered and prepared for injection. Hydroxyproline and proline were detected at 440 nm and other amino acids at 570 nm.

2.9. Circular dichroism (CD) analysis of protein structure

The effect of PCS on the secondary structure of plasma proteins was investigated using circular dichroism spectroscopy (Chirascan, Applied Photophysics Ltd, UK). Firstly, the background spectrum was recorded with ultrapure water as buffer solution. Plasma proteins solution was mixed with PCS solution and the final concentrations were 0.33 mg/mL and 1 mg/mL, respectively. The instrument parameters were set as follows: a 1 mm quartz cell path length was 1 mm, a time interval of 0.25 s, a detection wavelength range of 190–260 nm, and a scanning speed of 100 nm/min. The average spectrum of each group was obtained after three repeated measurements, and the CD spectra were calculated by deducting the background. The secondary structure content of proteins in each group was calculated by DichroWeb.

2.10. Binding kinetics for interactions of PCS and plasma proteins

The thermodynamic process of the binding between PCS and plasma proteins was investigated using an Isothermal Titration Calorimeter (MicroCal PEAQ-ITC, Malvern, UK). In each titration, 40 μL plasma proteins solution (40 μM) was injected into the protonated-chitosan solution (200 μL, 1 μM) at 25 °C, respectively. The binding heat was measured for each injection. The data was analyzed using a one-site binding model with a nonlinear least-squares fitting procedure and to determine the thermodynamic parameters (N, KD, ΔH, ΔG, -TΔS).

2.11. Molecular simulation

Molecular dynamics (MD) simulations were carried out by GROMACS 2020.3 software. The mechanism of molecular binding was obtained by simulating the interactions between negatively charged amino acids and positively charged $-NH_3^+$ group of chitosan molecular fragments. Detailed simulation procedures were provided in the supporting information.

2.12. Platelet adhesion, aggregation, activation, and secretion of coagulation substances

Platelet adhesion: 50 μL of platelet solution was applied to PCS sponge and incubated at 37 °C for 15 min. Non-adherent platelets were removed by washing with PBS three times. The adherent platelets were dehydrated by ethanol gradients (60 %, 70 %, 80 %, 90 % and 100 %), and the residual ethanol was naturally volatilized at room temperature. The adherent platelets were observed and imaged by FESEM (S-4800, Hitachi, Japan). The unprotonated-chitosan was served as the control group.

Platelet adhesion rate: Platelet adhesion rate was measured by LDH Elisa kit (Shanghai Yuduo Biotechnology Co., Ltd, China). In brief, after the incubation and rinsing, 100 μL of 1 % Triton-X was added to lysis of platelets, releasing lactate dehydrogenase. The OD value of the sample at 450 nm following the kit instructions. The blank group was treated with an equal amount of pure platelet lysis lysate for comparison. The adhesion rate was calculated as follows:

$$\text{Adhesion rate } (\%) = \frac{OD_{sample}}{OD_{Blank}} \times 100\%$$

Platelet activation and aggregation: Quantify platelet activation using flow cytometry (FACSJa22, BD, USA). Mixed 100 μL of PCS solution (5.0 mg/mL) with 100 μL platelet suspension and incubated at 37 °C for 10 min. Centrifuged the mixture at 3600 r/min for 5 min to allow platelet sedimentation. Removed the supernatant and added 0.5 mL of cell staining buffer (FITC anti-mouse/rat CD61, PE anti-mouse/rat CD62P, Biolegend) to the EP tube, and then incubated in dark for 1 h. Finally, analyzed platelet activation using flow cytometry, and repeated the process three times for each sample. In addition, the aggregation state of activated platelets was observed through confocal microscopy (LEICA TCS SP8, leicamicrosystem, Germany), with platelets labeled with FITC-CD61 and PE-CD62P.

Calcium Imaging: Platelets resuspended in cell staining buffer (37 °C) were incubated with 2 μM Fluo-8 AM (AAT Bioquest) for 30 min. Subsequently, PCS was added to platelet suspension, and platelet fluorescence signals were measured and observed by flow cytometry and confocal microscopy.

Secretion of intracellular coagulation substances in platelets: 100 μL PCS (5.0 mg/mL) was mixed with 100 μL platelet suspension, and incubated at 37 °C for 10 min. The concentration of coagulation substances(FV, FX, 5-TH, ADP) in the solution was quantitatively measured according to the Elisa kit operating instructions. Refer to the supporting materials for detailed steps.

2.13. PT/APTT test

Prothrombin time (PT) and activated partial thromboplastin time (APTT) were tested by a semi-automatic coagulation instrument (MC-2000, Germany).

APTT: 25 μL PCS solution, 25 μL PPP and 50 μL APTT test reagent were added to the test cup and mixed thoroughly. The mixture was incubated at 37 °C for 3 min. $CaCl_2$ (50 μL. 0.025 M) was then added and APTT data were registered. The PBS group was used as the control, and the measurements were measured four times for each group.

PT: 25 μL PCS solution and 25 μL PPP were added into the test cup, and preheated at 37 °C for 3 min. 100 μL PT test reagent was then added and PT data were collected. The PBS group was used as the control group, and the samples in each group were measured four times.

2.14. Protein analysis in protein clots

100 μL of PRP was mixed with 100 μL of PCS solution, followed by the addition of 10 μL of $CaCl_2$ (0.2 M) to initiate the coagulation reaction. After incubation at 37 °C for 10 min, the protein clots were separated and washed three times with PBS. The composition of the protein clots was analyzed using LC-MS/MS. The composition of coagulation factors in the supernatant (FV, FVII, FIX, FX, FXI, FXII, FXII, thrombin) was analyzed using the Elisa assay kit.

2.15. RBCs adhesion

100 μL of RBCs suspension was added into the PCS sponge (6 × 6 × 5 mm) and incubated it at 37 °C for 10 min. After washing three times with PBS, samples were fixed with a small amount of 2.5 % Glutaraldehyde for 10 min. 60 %, 70 %, 80 %, 90 %, and 100 % ethanol were used for step dehydration, followed by freeze-drying to evaporate the residual solvent. The surface morphology of RBCs was observed with FESEM (S-4800, Hitachi, Japan). The unprotonated-chitosan was served as the control group. The detailed procedure for the RBCs adhesion rate experiment was provided in the supporting information.

2.16. Blood coagulation index (BCI)

Dynamic blood coagulation index (BCI) was used to evaluate the hemostatic efficacy of the material *in vitro* [27,28]. The procedure followed a previously reported method. PCS (2 wt%) solution was injected into the 48-well plate to create cylindrical sponges with a diameter of 6 mm and a height of 5 mm.

100 μL anticoagulant blood and 10 μL $CaCl_2$ (0.2 M) were applied to PCS sponge and incubated in 37 °C water bath for 0.5, 1, 1.5, 2 and 2.5min, respectively. Celox™ and ChitoGauze®XR served as control groups. After each incubation period, 2 mL of deionized water was added to the sponge to lyse non-clotted red blood cells. The absorbance of the supernatant was read at 540 nm by a microplate reader (SpectraMax M2, Molecular Devices, USA), and the measurements were repeated for three times. A negative control group was prepared by adding 2 mL deionized water to 100 μL anticoagulant blood.

$$\text{BCI } (\%) = \frac{A_S - A_O}{A_{N-A_O}} \times 100\%$$

The absorbance of the sample, the negative control group, and the deionized water was represented as A_S, A_N, A_O.

2.17. Rheological analysis of blood clot

During the coagulation reaction, fibrin clots with stable mechanical properties were formed, effectively sealing the bleeding wound. Rheological properties of PCS-blood mixture were performed on a RL-MARS3 rheometer (Thermo Hakke, USA). All experiments were conducted at 25.0 °C using a 20.0 mm parallel plate with plate gap of 0.1 mm. 150 μL

anticoagulant whole blood and 10 μL $CaCl_2$ (0.2 M) were dripped into 5 mg sponge sample. Frequency sweeps were conducted at oscillation frequencies ranging from 0.1 to 10.0 Hz under a 5.0 % strain level. Strain sweeps were conducted at a fixed oscillation frequency of 1.0 Hz with variable applied strain from 0.1 to 100.0 %.

2.18. Hemolysis rate test

0.5 mL PCS (2.5 mg/mL, 5 mg/mL) was mixed with 0.5 mL RBCs suspension (5.0 v/v% in PBS). After the samples were incubated with RBCs for 1 h at 37 °C, followed by centrifugation at 1600 rpm/min, the absorbance of the supernatant was read at 540 nm by a microplate reader (SpectraMax M2, Molecular Devices, USA). PBS was used as a positive control and deionized water as a negative control. The hemolysis rate formula of the sample was as follows:

$$Haemolysis\ ratio\ (\%) = \frac{A_s - A_n}{A_p - A_n} \times 100\%$$

where A_s, A_n, A_p represented the absorbance of the sample, negative control, and positive control, respectively.

2.19. Cytocompatibility

The cytocompatibility of PCS was evaluated by CCK-8 and Live/Dead staining assays (Calcein/PI, Beyotime Biotechnology, Shanghai, China). Briefly, the PCS spomges were sterilized and immersed in DMEM at 5 mg/mL for 24 h. L929 cells were seeded in a 96-well plate at a density of 1.0×10^4 cells/well and cultured for 24 h. After the L929 cells were cultured for 24 h, the extract was added into the wells. To prepare for the assays, the culture medium in the wells was removed and the wells were rinsed three times with PBS to eliminate any residual medium. Cell viability was determined by CCK-8 and Live/Dead staining after co-cultured with the extract for 1 and 3 d. The culture medium in the well was removed and rinse with PBS three times to remove the residue. At each time point, the spent medium was discarded, and 100 μL fresh basic medium containing 10 μL CCK-8 reagent was added to each well. The plates were then incubated in a humidified incubator at 37.0 °C and 5.0 % CO_2 for 2 h. Finally, the absorbance was measured at 450 nm using a microplate reader (Multiskan Go, Thermo Scientific, USA). The assays were repeated four times for each group.

In addition, detailed steps for *in vivo* compatibility were provided in the supporting information.

2.20. Antibacterial capability

Escherichia coli (*E.coil*) and *Staphylococcus aureus* (*S. aureus*) were used to evaluate the resistance of PCS to gram negative and gram-positive bacteria. In short, bacteria were cultured in bacterial culture medium for 10 h until a saturated density of 10^9 CFU/mL was achieved. The PCS solution (2.5 mg/mL) was incubated with bacteria (10^6 CFU/mL) on a shaking table (80 rpm/min) at 37 °C for 30 min. After incubation, the mixture was diluted stepwise. A 100 μL of the mixture was spread onto the soybean agar plates and evenly distributed. The plates were incubated at 37 °C for 12 h, after which photos were taken and the number of bacterial colonies were calculated. The normal saline group was used as the control, and each group was replicated three times.

2.21. Hemostasis in vivo

The hemostatic efficacy of PCS95 was evaluated using animal models, which included rat liver resection, rat femoral artery hemorrhage and rabbit liver bleeding. Gauze, Celox™ and ChitoGauze®XR were used as control group, while PCS95 was used as the sample group.

In *vivo* hemostatic in a rat liver resection model: Pentobarbital sodium (40 mg/kg) was injected into each SD rat to induce complete anesthesia. The abdominal body hair was shaved off and a midline incision was made on the ventral side to expose the rat liver. Body fluid under the liver was absorbed with gauze, and a pre-weighed filter paper was placed under the liver. A section of the liver (2.5 cm × 1.0 cm × 0.5 cm) was cut off. After the blood flowed out, 500 mg of pre-weighed hemostatic dressing was applied to the wound to stop bleeding. The amount of bleeding was calculated by comparing the final weight of filter paper and dressing, and the total time of hemostasis was recorded.

To verify the bleeding effect of protonated chitosan on non-compressible wounds, a "cross" wound (1.5 cm × 1.5 cm × 0.3 cm) was made on the rat liver with a scalpel. After the blood was drained, PCS95 solution was injected into the wound and photographs were taken to document the bleeding control.

Rat femoral artery hemorrhage model: After anesthetizing and immobilizing Sprague-Dawley (SD) rats, the femoral artery was induced to rupture and bleed at the base using surgical scissors. Hemostatic materials were promptly applied to compress the bleeding site. The hemostasis process was recorded using an iPhone 13 smartphone.

Rabbit liver resection bleeding: Continuous injection of aspirin (2 mg/kg) was used to create an anticoagulant environment in the blood, which was evaluated by thrombelastograghy. An appropriate dose of pentobarbital sodium (40 mg/kg) was injected into each New Zealand White Rabbit (male, 2–2.5 kg) to induce complete anesthesia. The liver was carefully dissected from surrounding tissues and placed on a sterile filter paper substrate. A surgical incision was made approximately 1 cm above the liver's tip, causing liver bleeding. Hemostatic materials were then applied to the bleeding site to achieve hemostasis. The entire hemostasis process was visually documented using a high-resolution camera, allowing for the recording of hemostasis time. Additionally, the blood loss during hemostasis was quantified by weighing the collected blood.

2.22. Statistical analysis

A sample size of $N \geq 3$ was used for all experiments. Data are shown as mean ± s.d. Statistical analysis was performed using one-way ANOVA and post hoc Tukey tests formultiple comparisons or Student's t-tests for comparison between two groups (Prism 8.0.2). P values < 0.05 were considered statistically significant (*$P < 0.05$, **$P < 0.01$, ***$P < 0.001$, ****$P < 0.0001$).

3. Results

3.1. Preparation and characterization of PCS95, PCS80 and PCS65

Chitosan is a linear polymer rich in amino and hydroxyl groups, derived from the shells of shrimp, crab and other marine arthropods. Under acidic conditions, the $–NH_2$ groups in chitosan molecules are protonated to form $–NH_3^+$ groups. The biological activity of chitosan is affected by molecular weight, deacetylation degree, viscosity and other factors [29,30].

In experiment, we observed an unexpected phenomenon where the addition of a protonated-chitosan solution to plasma proteins promptly led to the formation of a protein membrane. Further experiments indicated that the phenomenon was related to the amount of $–NH_3^+$ group. A higher the deacetylation degree of protonated-chitosan molecules corresponds to a greater number of positively charged amino groups ($-NH_3^+$). To explore the interaction between chitosan and blood and reduce the interference of unnecessary factors, the 95 % deacetylated chitosan was grafted with acetic acid via EDC·HCl coupling to obtain protonated chitosan with deacetylation degrees of 80 % (PCS80) and 65 % (PCS65).

Fig. 1a depicted the synthesis process, where PCS80 and PCS65 were synthesized by adjusting the feeding ratio (Table S1). The chemical structure of protonated-chitosan was confirmed by ATR-FTIR spectroscopy (Fig. 1b), with the absorption peak at 1640 cm^{-1} corresponding to

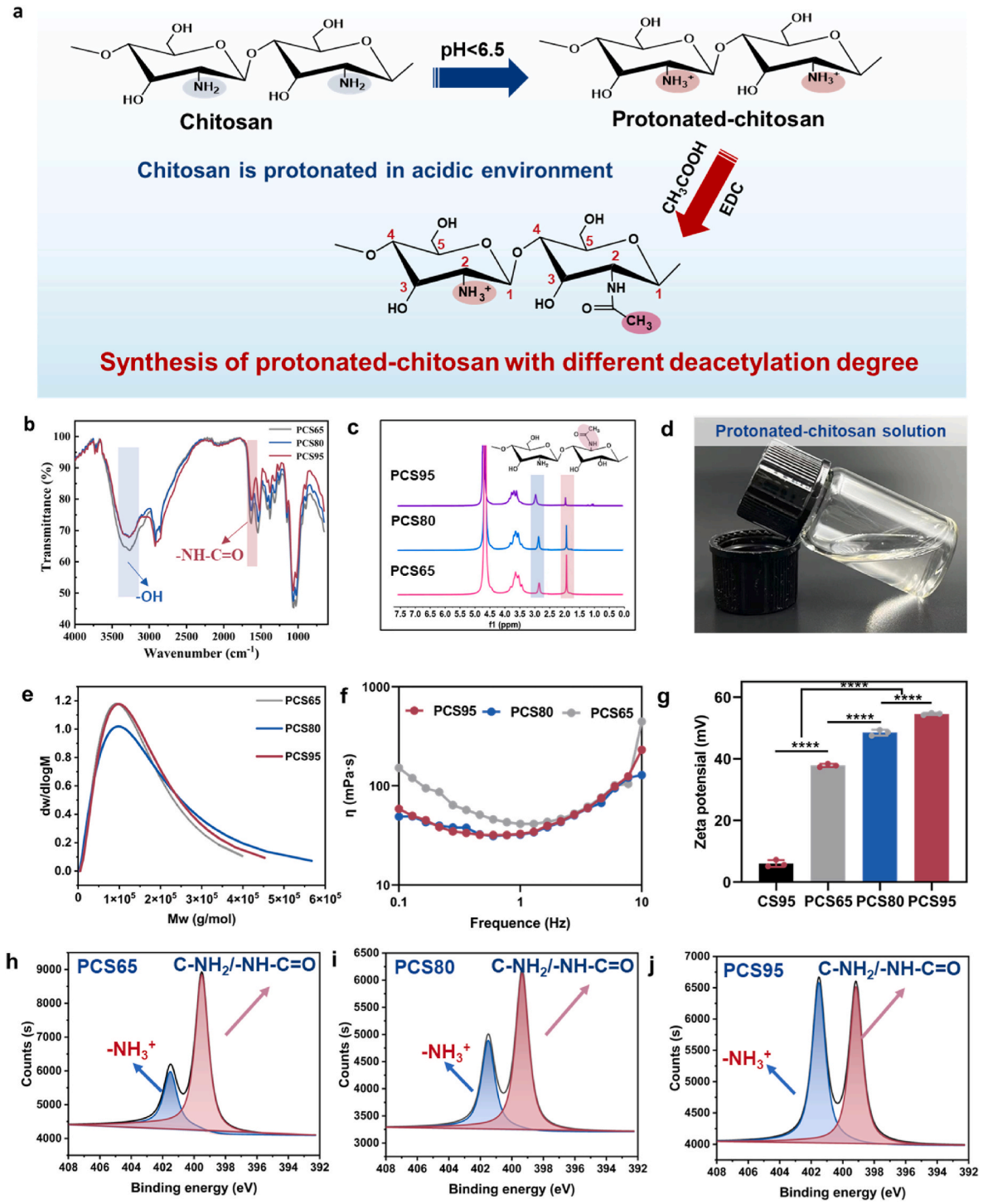

Fig. 1. Structural and physical properties of PCS with different deacetylation degrees. a) The synthesis process and schematic diagram of PCS. b) ATR-FTIR spectra of PCS. c) ^{1}H NMR (D_2O, 600 MHz) spectra of PCS. d) Photographs of protonated-chitosan solution (2.0 wt%). e) Gel permeation chromatography (GPC) of PCS. f) Rheological analysis of PCS at a frequency range from 0 to 10 Hz. g) Zeta potential of PCS (n = 3, ****p < 0.0001). h-j) N1s XPS spectra of PCS65, PCS80 and PCS95 (blue area represents the peak of $-NH_3^+$, red area represents the peak of C–NH_2/-NH-C=O).

-NH-C=O of protonated-chitosan. As the grafting rate of acetic acid molecules increased, the intensity of the absorption peak increased. The degree of conjugation of acetic acid was confirmed by proton nuclear magnetic resonance (^{1}H NMR) spectrometer (Fig. 1c). The proton peak at 1.95 ppm represents the methyl group (-CH_3) of protonated-chitosan molecule, and the proton peak at 2.95 ppm corresponded to C_2–H bond in protonated-chitosan. By integrating the proton peak areas, the deacetylation degree of PCS95, PCS80, and PCS65 were calculated to be 95.6 %, 80.3 %, and 65.4 %, respectively. In addition, chitosan is insoluble under neutral conditions, but protonated-chitosan exhibited excellent solubility in deionized water with a solubility exceeding 20 mg/mL (Fig. 1d), significantly expanding the applications of chitosan-based materials. The molecular weight of PCS variants was characterized by gel permeation chromatography (GPC), with the average molecular weights of PCS65, PCS80, and PCS95 being relatively similar of 11.2 kDa, 10.4 kDa, and 11.6 kDa, respectively (Fig. 1e). The viscosities

of the three PCS were relatively close (Fig. 1f), with values of 32.8, 32.2 and 41.4 mPa·s (1 Hz), respectively. Furthmore, zeta potential and XPS were employed to characterize the charge-carrying capacity of $–NH_3^+$groups in the protonated-chitosan molecular chain. The zeta potential for PCS95, PCS80 and PCS65 were 54.6 ± 0.2 mV, 48.5 ± 0.7 mV and 39.2 ± 0.5 mV, respectively. In contrast, the zeta potential for unprotonated-chitosan (CS95, 95 % deacetylated) was significantly lower at 6.0 ± 0.9 mV (Fig. 1g). Moreover, the peaks at 399.8 eV and 401.1 eV were attributed to C–NH_2/-NH-C=O and $–NH_3^+$ [31], respectively. However, unprotonated-chitosan (CS95, 95 % deacetylated) lacked a significant peak at 401.1 eV (Fig. S1). As the deacetylation degree of chitosan increased, the number of positively charged $–NH_3^+$ groups also increased. The ratio of $–NH_3^+$ group peak area to the total peak area was 25.3 % for PCS65, 35.5 % for PCS80, and 49.7 % for PCS95, respectively (Fig. 1h–j). In conclusion, we have successfully synthesized protonated-chitosan with varying degrees of deacetylation (PCS95, PCS80, PCS65), maintaining consistent molecular weight and viscosity.

3.2. Interaction between protonated-chitosan and plasma proteins

Blood is a complex mixture rich in abundant proteins (such as albumin, immunoglobulins, complement proteins, coagulation proteins, etc.), cells (erythrocytes, platelets, white blood cells, etc.), ions (Ca^{2+}, K^+, Na^+, Cl^-, etc.) and water. These components are essential for the transportation of nutrients and metabolites, immune response, clotting, regulation of temperature, and maintenance of physiological homeostasis. Upon intravenous injection, nano materials adsorb a certain amount of plasma proteins on their surfaces, forming a protein corona [32]. This phenomenon was called the “Vroman Effect” [33]. The composition of the protein corona (including lipoproteins, coagulation factors, and immunoglobulins, etc.) was affected by the surface charge, hydrophilicity and active functional groups (such as –COOH, –NH_2) on the nanoparticles [34,35]. In the experiment, we observed an unexpected robust adsorption of plasma proteins by positively charged chitosan, which quickly formed protein membrane within seconds (Mov. S1). We hypothesized that the formation of this protein membrane significantly impacted the coagulation process.

3.2.1. Formation conditions of Protein membrane

Firstly, we explored the conditions that lead to the formation of PM. Plasma proteins solution exhibited pH-responsive characteristics, with protein molecules carrying different charges depending on the pH level (Fig. S2). Specifically, when the pH of the solution surpassed the average isoelectric point (pH 5.4) [36], plasma proteins acquired negative charge. Conversely, when the pH fell below 5.4, the plasma proteins become positively charged. This phenomenon was attributed to the ionization of specific amino acid residues within the protein in response to pH changes. Under physiological conditions (pH 7.4), plasma proteins were negatively charged, with zeta potential of approximately −16 ± 0.3 mV (Fig. S2). Chitosan molecules are naturally cationic polymers, and their charge density depends on the degree of deacetylation and protonation [37]. The higher deacetylation of chitosan, the greater the number of available amino groups along molecular chain. For fully deacetylated chitosan, the theoretical amino group content is 6.2 mmol/g. In acid solution, the amino group is protonated to $–NH_3^+$. Therefore, we speculated that this phenomenon was related to the interaction between the positively charged protonated-chitosan molecules, and the negatively charged protein molecules to form protein membrane.

Chitosan with varying degrees of deacetylation (PCS95, PCS80, PCS65) exhibited a modest reduction in zeta potential within the pH range of 2–4 (Figs. S3a–c). However, when the pH increased to 7.4, the decrease in H^+ concentration, led to deprotonation of chitosan, and a significant decrease in zeta potential (<10 mV). Interestingly, protonated-chitosan with a high deacetylation degree (95 % deacetylation, pH = 2 and pH = 4) formed a dense protein membrane. When the zeta potential of protonated-chitosan (95 % deacetylation) decreased to 29 ± 0.2 mV (pH = 6), only turbidity was observed in the PPP solution, indicating that the deprotonation of chitosan led to a reduced binding capacity with proteins (Fig. S3d).

When chitosan solution (80 % deacetylation) was at pH 2 and 4, the addition of plasma proteins solution resulted in the formation of a flocculent protein membranes (Fig. S3e).

However, when the solution pH of chitosan (80 % deacetylated) was adjusted to 6, no protein membrane was observed. In addition, protonated-chitosan with lower deacetylation degree (65 % deacetylated) did not observe the protein membrane phenomenon under any pH conditions (Fig. S3f).

These results indicated that the formation of protein membrane was closely related to the deacetylation degree and protonation level of chitosan. Furthermore, when positively charged PEI (ζ = +13.4 ± 0.9 mV) and polylysine (ζ = +22.0 ± 2.2 mV) were added to plasma (Fig. S4a), no formation of protein membrane was observed (Fig. S4b). This is primarily due to the fact that, despite these molecules possessing positive charges, their charge density was relatively low, insufficient to interact with plasma proteins and form protein membrane.

Conversely, when the pH of plasma proteins solution was lowered to 2, resulting in a positively charged plasma protein solution, and the addition of negatively charged sodium alginate (ζ = −63.6 ± 1.3 mV) solution (Fig. S4c), led to observable protein membrane (Fig. S4d). However, the introduction of negatively charged hyaluronic acid (ζ = −36.6 ± 0.2 mV) and gelatin solution (ζ = −15.1 ± 0.5 mV) to positively charged plasma proteins solution did not observe this phenomenon. The phenomenon indicated that only materials with high charge density will interact with the plasma protein to produce protein membrane.

In summary, we explored the conditions for the protein membrane formation and confirmed that the phenomenon was mainly driven by the electrostatic interactions between PCS and plasma protein molecules. The higher the charge density of PCS molecules, the stronger their binding affinity with plasma proteins.

3.2.2. Analysis of protein membrane components

In the experiments exploring the conditions for PM formation, we confirmed that PCS95 exhibited the strongest binding affinity to plasma proteins. We introduced a PCS solution (2 wt%) to poor-platelet plasma (PPP) and observed that PCS95 quickly assembled proteins in plasma to form a protein membrane (PM) (Fig. 2a). The proteins in PM were separated by centrifugation for subsequent analysis (Fig. 2b). To analyze the protein composition of the PM, SDS-PAGE gel electrophoresis was employed to separate the proteins in PM from PPP. The molecular weight distribution of plasma proteins isolated from PM ranged widely, from 6.5 kDa to 270 kDa (Fig. 2c). The protein content (52 ~ 95 kDa) in PM was significantly lower than that in PPP, suggesting that PCS95 has the capacity to selectively adsorb proteins from plasma. For a quantitative analysis of the PM components, liquid chromatography coupled with mass spectrometry (LC-MS/MS) was utilized. The top 30 high abundance proteins account for approximately 67.98 % (PPP) and 60.95 % (PM) of the total protein content. Albumin, the most abundant protein in the PPP at 12 %, was present at only 2.3 % in the PM (Fig. 2d). A total of 165 differentially expressed proteins were detected in PPP and PM (Fig. 2e). Significantly, a number of coagulation-related proteins, including Factor II (FII), V (FV), VII (FVII), VIII (FVIII), IX (FIX), X (FX), XIII (FXIII), Fibronectin 1 (Fn1), VWF and Platelet Factor 4 (PF4), were detected in the PM and PPP. The abundance of various coagulation factors in PM were significantly higher than in PPP. The total abundance of coagulation factors increased from 1.09 % in the PPP to 2.59 % (Fig. 2f), indicating that PCS had a substantial recruitment effect on coagulation factors present in the blood. Specifically, except for a few coagulation factors such as FXI, FXII and VWF, the majority of clotting-related proteins were detected to be enriched in PM, approximately

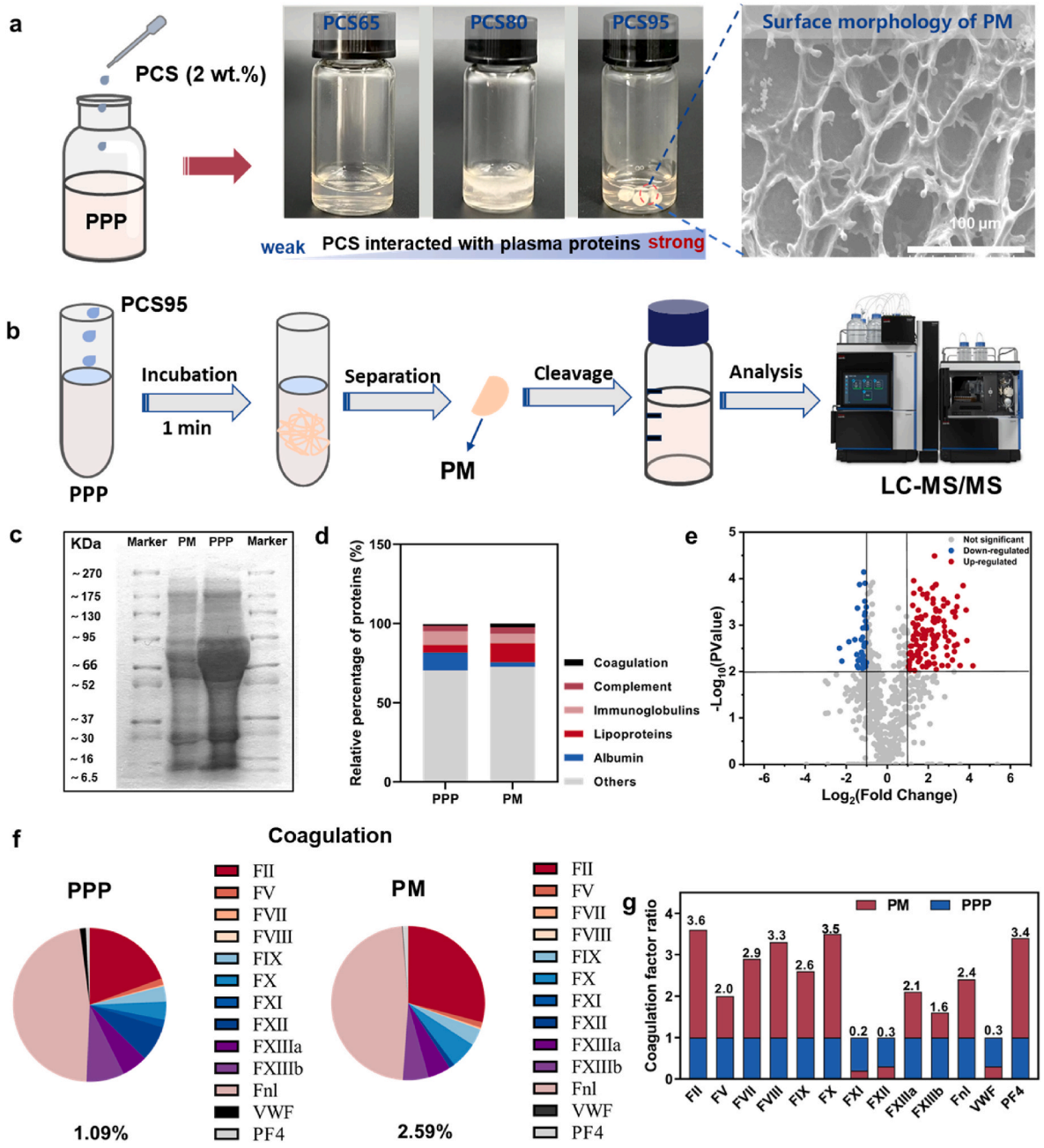

Fig. 2. PCS interacted with plasma proteins and Protein membrane component analysis. a) Photos and SEM image of protein membrane (PM). b) The process of PM sample processing. c) SDS-PAGE image of PPP and PM. d) Distribution of main proteins in PPP and PM. e) Volcanic maps showing PM up-regulated and down-regulated proteins relative to PPP. f) Coagulation related factors detected in PPP and PM. g) Enrichment ratio of coagulation-related factor abundance.

1.5–4 times higher than those in PPP (Fig. 2g). Since FXI carries an overall positive charge [38], its affinity for PCS, which is also positively charged, might have been weaker, potentially explaining its lower enrichment in PM. Similarly, VWF tends to bind with negatively charged materials such as collagen and sulfatides [39]. Moreover, FXII is known to have a high affinity for negatively charged substances, as it is readily activated by negatively charged surfaces to form FXIIa [40]. The assembly of plasma proteins enhanced the viscoelasticity of the material matrix and was conducive to platelet adhesion, aggregation and activation [41]. The recruitment of FIX by PCS would help to activated platelet cutting FIX to FIXa to accelerate the coagulation cascade. Additional protein information was provided in Fig. S5. In a word, PCS played a pivotal role in the intricate process of regulating and maintaining clot formation and stability by assembling plasma proteins and recruiting coagulation factors.

3.2.3. *Interaction mechanism between PCS and plasma proteins*

The molecule interaction process between PCS and plasma proteins was further investigated by isothermal titration calorimetry (ITC), circular dichroism (CD), amino acid analyzers, and molecular simulations.

Firstly, ITC, widely used for probing ligand-biomolecule interactions, was employed to analyze the thermodynamics of PCS binding to plasma protein. The detailed data were presented in Table S2. The interaction between PCS and plasma proteins was an endothermic reaction ($\Delta H>0$) at 25 °C, occurred spontaneously ($\Delta G<0$). For PCS65, maximum binding to plasma proteins was observed at 4 min post-titration, with saturation achieved by 32 min (Fig. 3a). For PCS80, optimal binding was observed at 8 min (Fig. 3b), with saturation reached by the 40-min mark. PCS95

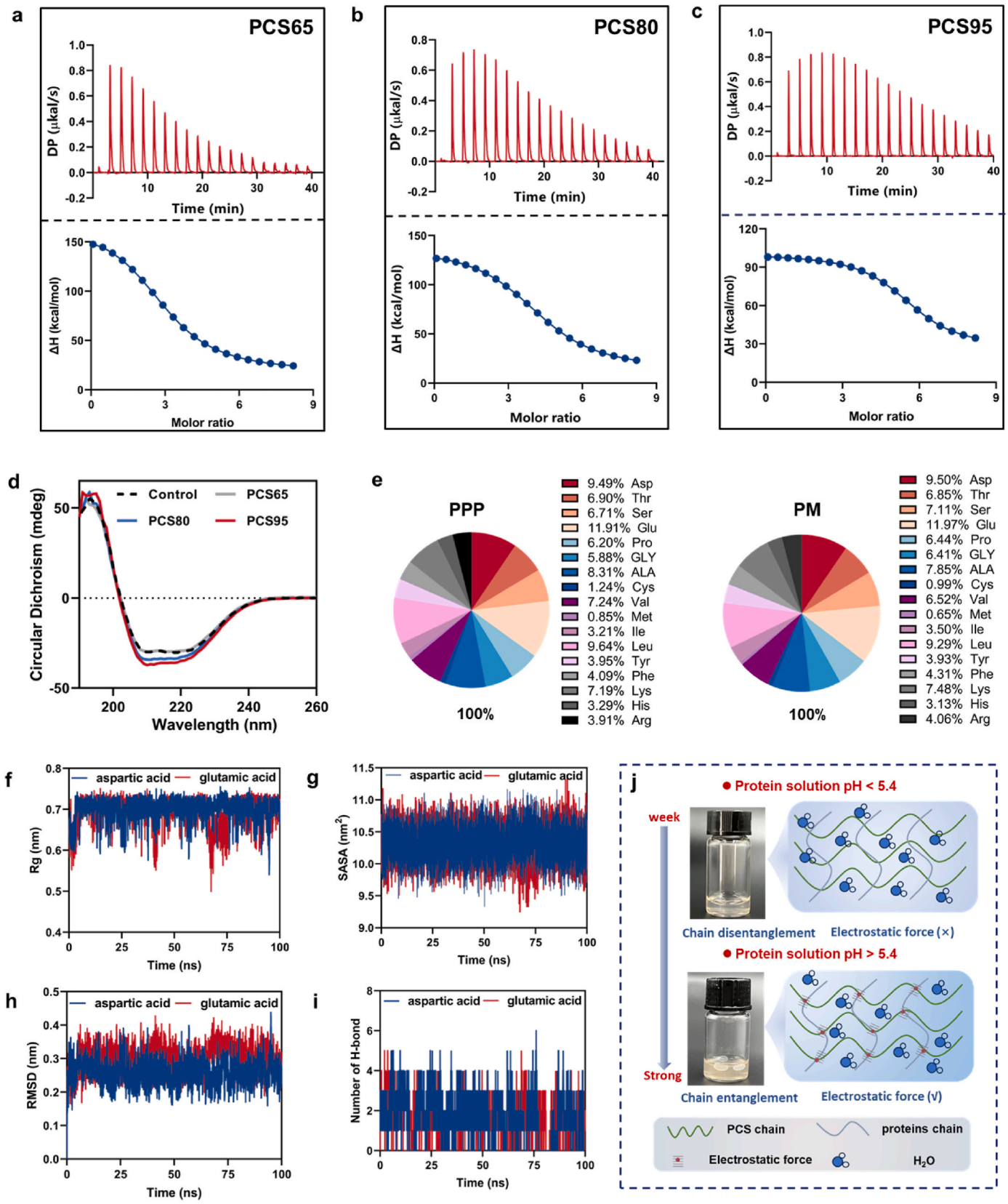

Fig. 3. Characterization of the interaction between PCS and plasma proteins. a-c) Isothermal Titration Calorimetry (ITC) analysis of the interaction between PCS65, PCS80, PCS95 and blood protein. d) Protein secondary structure analysis after the interaction between PCS and blood protein. e) PPP and PM amino acid composition analysis. f) The molecular Radius of Gyration (Rg) during molecular bonding. g) The solvent accessible surface area (SASA) of the molecular binding process. h) RMSD is Root Mean Square Deviation, which quantifies the spatial variation of molecularstructures. i) The number of hydrogen bonds in molecular bonding. j) Schematic diagram of the interaction between PCS and plasma proteins at different state of charge (pH = 5.4, pH = 7.4).

demonstrated maximum binding affinity to plasma proteins at 10 min post-titration. Even after 40 min of titration, the binding remained non-saturable (Fig. 3c). Moreover, a higher stoichiometric ratio (N) and more negative Gibbs energy (ΔG) indicated higher affinity [42]. PCS95 showed the highest stoichiometric ratio to PPP at 5.72, with the lowest gibbs energy at −8.85 kcal/mol. These results demonstrated that PCS95 exhibited the highest affinity for plasma proteins binding. The binding enthalpy (ΔH), which represented the intensity of hydrogen bonding and van der Waals forces, was notably low for PCS95 with plasma proteins, at 89.50 kcal/mol, suggesting that the binding between PCS and plasma proteins was predominantly charge-driven. A higher charge density of PCS molecule correlates with a stronger binding affinity to plasma proteins.

CD was employed to analyze the changes in secondary protein structure during PCS and plasma protein interactions (Fig. 3d). PCS had a minimal impact on the secondary structure of plasma proteins. There was a slight increase in the α-helix, β-sheet, and β-turn structures (Table S3), with the levels of random coils remaining constant. These results suggested that PCS did not disrupt the structural integrity of plasma protein's, which maintained their conformational stability and biological activity upon interaction with PCS. Moreover, the stability of the secondary structure conformation of membrane proteins reduced the risk of immune responses in practical applications of PCS [43].

In experiments, we observed that PCS95 formed protein membrane by binding with plasma proteins under physiological conditions. However, when the pH of the PPP solution was adjusted below its isoelectric point, PPP became positively charged, and the formation of the protein membrane was not observed (Fig. 3j). Amino acids in proteins were further evaluated by an amino acid analyzer from PPP and PM. Proteins are mainly composed of 17 different amino acid molecules, with positively charged amino acids including arginine, lysine, and histidine, and negatively charged amino acids liking glutamic acid and aspartic acid. The most abundant amino acids hydrolyzed from PM were glutamic acid and aspartic acid, with the total content of negatively charged amino acids in PM accounting for 21.47 %, which was already close to the saturation level of negatively charged amino acids found in PPP (Fig. 3e). The above results indicated that the formation of protein membranes was mainly due to the binding of negatively charged amino acids to positively charged protonated-chitosan.

To further elucidate the interaction between PCS and plasma proteins, molecular dynamics (MD) simulations were performed. We simulated the binding of these negatively charged amino acids to protonated chitosan structural unit fragments. The MD simulations, revealed stable binding between PCS and plasma proteins, mediated by a combination of electrostatic, van der Waals, and hydrophobic interactions. In this process, root mean square deviation (RMSD), solvent accessible surface area (SASA), and the molecular radius of gyration (Rg) reached a plateau state and are stabilized within 10 ns (Fig. 3f–i), demonstrating rapid interaction between PCS and amino acids. At the isoelectric point, plasma protein molecules are electrically neutral, and the binding energies of PCS with amino acids are low (Fig. S6, Table S4a), being −0.9 kJ/mol for aspartic acid and −5.1 kJ/mol for glutamic acid, respectively. Under physiological conditions (pH = 7.4), the carboxyl groups of these amino acids ionize to release H^+, and the –COOH groups ionized to -COO^-. In such conditions, the primary binding force between PCS and these amino acids was electrostatic interaction (Table S4b). The total binding energies with these two amino acids were −278.0 kJ/mol for aspartic acid and −290.7 kJ/mol for glutamic acid, respectively. The simulation results were consistent with the previously observed phenomena.

In summary, under physiological conditions, ionization of H^+ by aspartic acid and glutamate in plasma protein molecular chains imparts a negative charge to plasma protein solution. PCS molecular chains with $–NH_3^+$ groups and plasma protein molecular chains tangle with each other to spontaneously form PM driven by electrostatic action (Fig. 3j).

3.3. Platelet adhesion, activation, aggregation and secretion by PCS

Platelets play a crucial role in the hemostasis process. A deficiency or dysfunction of platelets can lead to various coagulation disorders. Platelets are highly active secretory cells, platelets respond to external stimuli by activating surface receptors ($P2Y_{12}$, PAR1/PAR4, CLEC2, TLR, etc.), and triggering signaling pathways [2,44,45]. This leads to the secretion of growth factors, inflammatory factors, coagulation factors, and extracellular vesicles into the bloodstream, which modulate the blood microenvironment [46]. These intracellular components interact and regulate platelet function during hemostasis. The cell-based coagulation model [47], emphasizes the crucial role of platelets in the coagulation process. Initially, coagulation factors bind to membrane receptors on resting platelets. Once platelets are activated, they provide additional binding sites for the rection of coagulation cascade. In this study, we explored the effect of PCS on platelet adhesion, aggregation and activation and the subsequent secretion of coagulation-related substance.

Firstly, SEM imaging revealed that PCS95, with its high charge density, attracted the largest number of adhered platelets (Fig. 4a, Fig. S7). The platelet adhesion rate on PCS sponges was further quantitatively analyzed by LDH Elisa kit. Consistent with the SEM observations, PCS95 demonstrated the highest platelet adhesion rate of 64.9 % ± 3.3 % (Fig. S7). In addition, PCS treatment led to platelets activation, leading to an increased expression of platelet receptor CD62P and CD61 [48]. The platelet activation rates for PCS65, PCS80 and PCS95 were 7.8 ± 0.6 %, 74.7 ± 0.8 % and 96.3 ± 0.3 %, respectively, compared to only 2.1 ± 0.2 % for the control group (Fig. 4b and c). More importantly, in the presence of anti-platelet drugs (like aspirin, eptifibatide, etc.), PCS95 maintained an extremely high level of platelet activation and the activation rate is more than 70 % (Fig. S8). The results were related to chitosan's activation of the platelet Toll-like receptor 2, a receptor that was not subject to the intervention of antiplatelet drugs [2]. Moreover, intracellular calcium signaling is essential for platelet function [49]. Upon platelet activation, a rapid increase in cytosolic calcium concentration occurs, primarily driven by the release of calcium from intracellular stores and subsequent influx of extracellular calcium. After platelets activated by PCS, an increase in intracellular calcium ion concentration was observed using flow cytometry (Fig. 4d and e). Moreover, confocal microscopy confirmed different degrees of platelet aggregation, with PCS95 having the most pronounced effect (Fig. 4f and g). The results attributed to the activation of platelet surface integrin receptors by PCS95, promoting the aggregation of platelets.

The α-granules within platelets are repositories for Platelet Factor 4 (PF4), and coagulation factors such as FV, FX, and FXI [50]. PF4 is known to enhance platelet aggregation and bind to heparin, neutralizing the anticoagulant effect [51]. When PCS95 interacted with platelets, the PF4 concentration increased about three-fold compared to the control group (Fig. 4h). The secretion of intracellular clotting factors from platelets significantly boosted their concentration in the bloodstream, thereby accelerating coagulation reactions. Unlike FV in plasma, FV in platelet was secreted in a semi-activated state after platelet stimulation. It showcases significant cofactor activity, which is further enhanced by a factor of two to three upon activation via thrombin or Factor Xa [52]. Elisa detected a significant increase in FV concentration with the PCS95 sample showing a FV concentration of 783 ± 19 ng/mL approximately 5.8 times higher than the control group (Fig. 4i). Similarly, significant increase in the concentrations of FX (Fig. 4j) and FXI (Fig. 4k) were detected with PCS95 levels 6 and 5.7 times higher than the control, respectively. These results underscore the potential of platelet-derived clotting factor release to enhance the clotting factors concentration in the blood, thereby promoting rapid coagulation reactions.

Additionally, platelet activation, triggers the secretion of dense granules, which contain small molecules such as ADP and 5-HT (serotonin) [53]. These molecules play a pivotal role in recruiting platelets to the bleeding site and amplifying the platelet response. After interaction

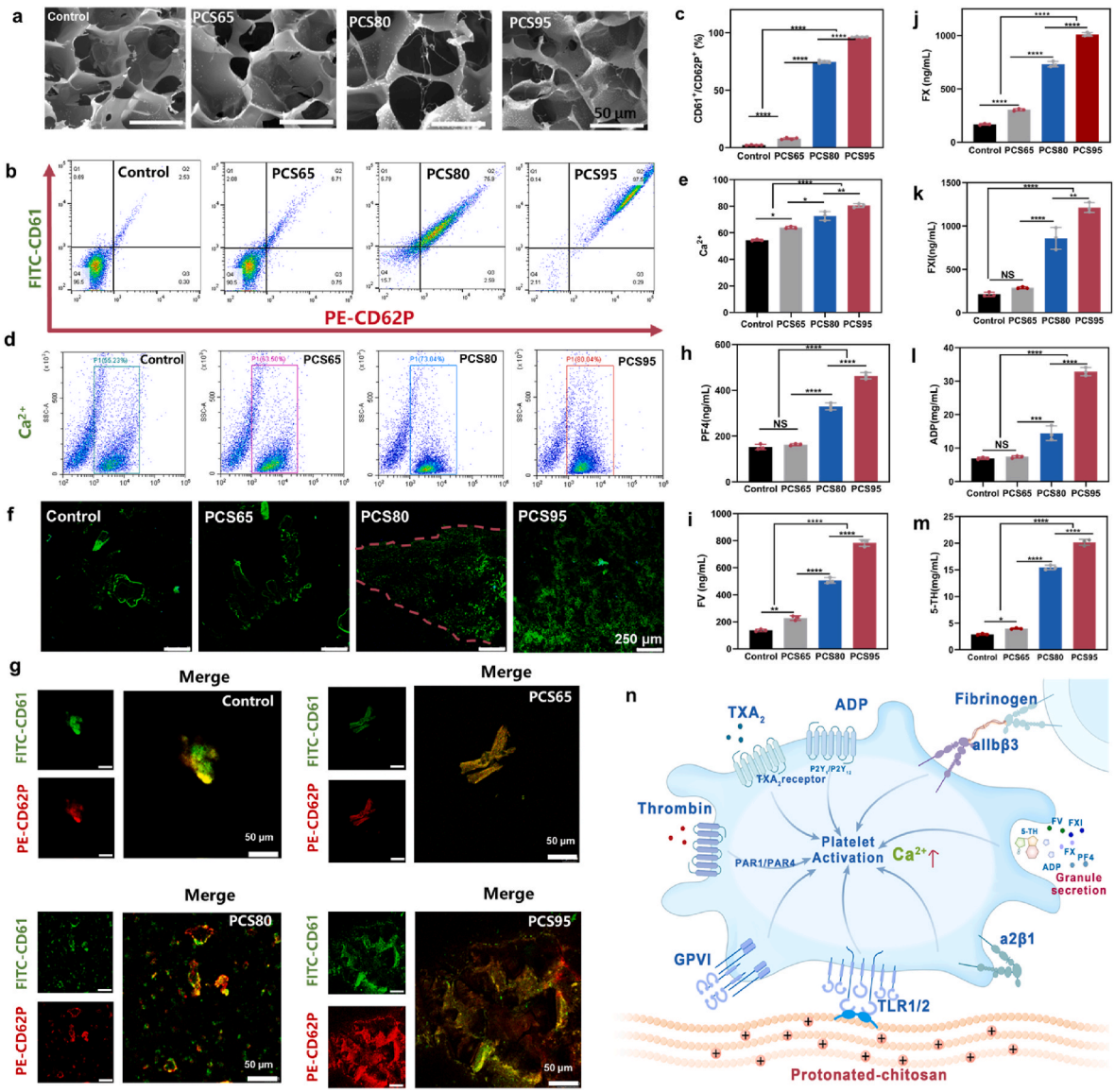

Fig. 4. PCS interacted with platelets. a) SEM image of platelets adhesion (Scale bar: 50 μm). b) Flow cytometry analysis diagram of platelet activation ($CD61^+$/$CD62p^+$) of PCS (n = 3). c) Platelet activation rate of platelets after exposure to PCS solution ($CD61^+$/$CD62p^+$), n = 3. d) Flow cytometry analysis of intracellular platelet calcium ion (n = 3). e) Relative content of intracellular calcium ion concentration in platelets. f) Confocal image of platelet aggregation (Ca^{2+}, Scale bar: 250 μm). g) Confocal picture of platelet activation and aggregation (FITC-CD61/PE-CD62P, Scale bar: 50 μm). h-k) The platelets secreted concentration of PF4, FV, FX, FXI respectively (n = 3). l) The concentration of ADP secreted extracellularly by platelets (n = 3). m) The concentration of 5-TH secreted extracellularly by platelets (n = 3). n) Schematic diagram of the interaction between PCS and platelets (NS, no significant differences, *P < 0.05, **P < 0.01, ***P < 0.001, ****P < 0.0001).

with protonated chitosan, ADP, 5-TH concentrations increased (Fig. 4l and m), with the PCS95 group showing a 4.8-fold (32.8 ± 0.8 mg/mL) and 7.1-fold (20.1 ± 0.4 mg/mL) increase respectively, compared to the control group. Interestingly, we also observed that after PCS95 activated platelets, it released some activated platelets into the solution, which could help accelerate blood coagulation around the material (Fig. S9).

In summary, platelets play a pivotal role in hemostasis regulation, serving as a reservoir for clotting factors and fostering a procoagulant environment. The activation capability of PCS towards platelets was associated with the $-NH_3^+$ groups; the greater the number of $-NH_3^+$ groups, the stronger the ability of PCS to activate platelets. PCS incubation induced platelet activation, resulting in the secretion of intracellular coagulation components. Additionally, activated platelets served as catalytic sites for the amplification of coagulation cascade through the intricate interaction of various coagulation factors (Fig. 4n).

3.4. Hemostatic mechanism of PCS

The physiological coagulation process is a complex biochemical cascade that involves multitude of coagulation factors and cellular components. The activation of intrinsic and extrinsic coagulation pathways initiates a chain of reactions that culminate in the assembly of prothrombinase complexes on platelet surfaces [54]. This process ultimately leads to the crosslinking of fibrinogen molecules and the formation of insoluble fibrin clots [55].

Firstly, PT and APTT tests revealed that PCS exerted a relatively minor influence on the initiation of both the intrinsic and extrinsic coagulation pathways (Fig. 5a and b).

In study, we found that PCS could recruit coagulation factors and assemble plasma proteins from PPP, as well as adhere to and activate platelets, the secretion of intracellular coagulation substances. To evaluate the ability of PCS to induce protein clots formation, we incubated it with platelet-rich plasma (PRP) and added $CaCl_2$ to initiate the

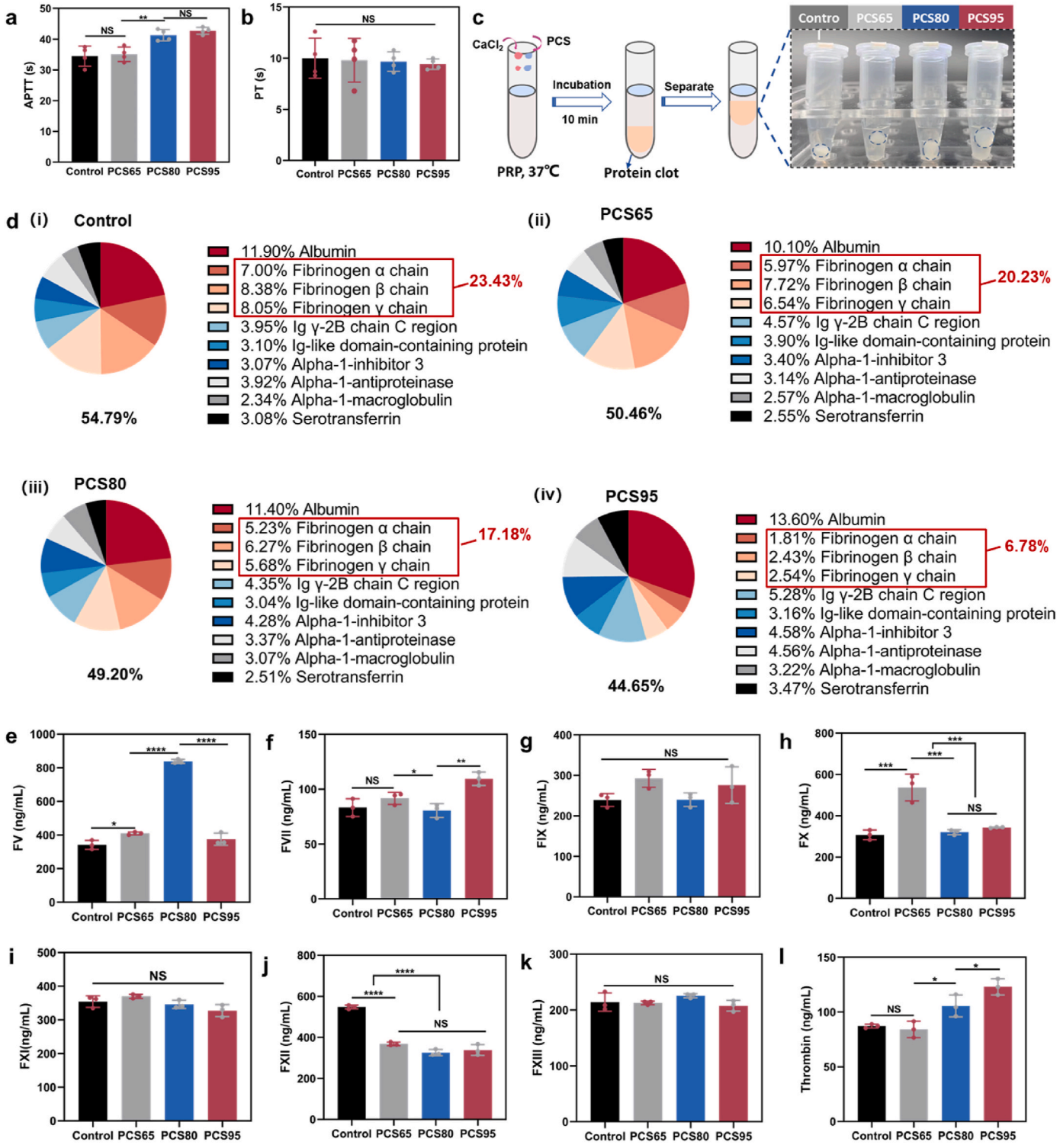

Fig. 5. Proteomics analysis of protein clots. a, b) PT/APTT testing of PCS. c) Photographs showing the interaction of PCS interacted with PRP to form protein clots. d) The top 10 protein abundances in protein clots. e-l) Concentration of unreacted coagulation factors (FV, FVII, FIX, FX, FXI, FXII, FXIII, thrombin) in the supernatant (n = 3). (NS, no significant differences, *P < 0.05, **P < 0.01, ***P < 0.001, ****P < 0.0001).

coagulation cascade reaction.

Upon completion of the reaction, we observed that the control group produced the smallest protein clot, while the PCS95 group yielded the largest clot with the least amount of supernatant remaining (Fig. 5c), suggesting that PCS95 exhibited superior hemostatic performance. Proteomic analysis of the formed blood clots revealed that albumin was the most abundant protein, accounting for approximately 10~14 % of the total protein content. The protein clots also contained abundant fibrinogen chain, including fibrinogen α, β and γ chains (Fig. 5d). Interestingly, the blank group exhibited the highest proportion of fibrinogen, reaching 23.43 %, whereas the PCS95 group had lower fibrinogen content of 6.78 %. This was mainly due to PCS's effectiveness in assembling a large amount of plasma proteins into the fibrin matrix, which decreases the content of fibrin. Moreover, unreacted coagulation

factors such as FII, FV, FVII, FIX, FXI, FXII and FXII were detected in protein clots. The total coagulation factor content for the control, PCS65, PCS80 and PCS95 groups were 0.83 %, 0.77 %, 0.73 % and 0.70 %, respectively. Further details about proteins were provided in Fig. S10.

After the hemostatic response reached equilibrium, the concentrations of coagulation factors FV, FVII, FIX, FX, FXI, FXII, FXII and thrombin in the supernatant were determined by Elisa assays (Fig. 5e-l). The different groups demonstrated varied consumption of coagulation factors, with the PCS80 group exhibiting relatively higher remaining levels of coagulation factor FV. The PCS65 group had increased residual FX (536.7 ± 48.6 ng/mL), while the control group had higher residual FXII (547.9 ± 6.7 ng/mL). In addition, no significant differences were observed in the residual amount of FVII and FIX among all groups.

Based on our aforementioned research on the interactions between PCS and PPP, platelets, and PRP, we have observed that the interactions between PCS and these blood elements are both sequential and dynamic. Hence, we propose a "three-stage rocket" model for PCS to facilitate rapid coagulation and hemostasis: First, PCS recruits coagulation factors and electrostatically assembles high-abundance plasma proteins to form an initial protein network within few secends. Secondly, protein network and PCS mediate platelet activation, leading to the secretion coagulation substances from platelets, and establishing reaction sites for coagulation factor to produce thrombin. The third stage involved coagulation factors reacting on the platelet surface to produce thrombin, which cleaves fibrinogen to form fibrin, creating an insoluble fibrin network.

3.5. Hemostatic properties in vitro

Erythrocytes are the most abundant cells in the blood, and during the coagulation cascade, their encapsulation in a fibrin network, which is crucial for enhancing the mechanical stability of the blood clot [56]. Therefore, the adhesion and aggregation of erythrocytes are pivotal in the formation of stable blood clot. SEM images revealed that PCS95 adhered the highest number of erythrocytes (Fig. 6a), with an adhesion rate exceeding 50 % (Fig. 6b).

Hemostatic materials function by absorbing blood at the site, facilitating the formation of a stable blood clot, thereby plugging the wound and achieving hemostasis. The *in vitro* hemostatic capability of these materials could be assessed by monitoring the change in the blood coagulation index over time (Fig. 6c). A lower BCI value, signifies a more potent ability to stop bleeding. The chitosan-based commercial hemostatic products Celox™ and ChitoGauze®XR were used as control groups. As shown in Fig. 6d, blood clots formed by interaction of PCS95

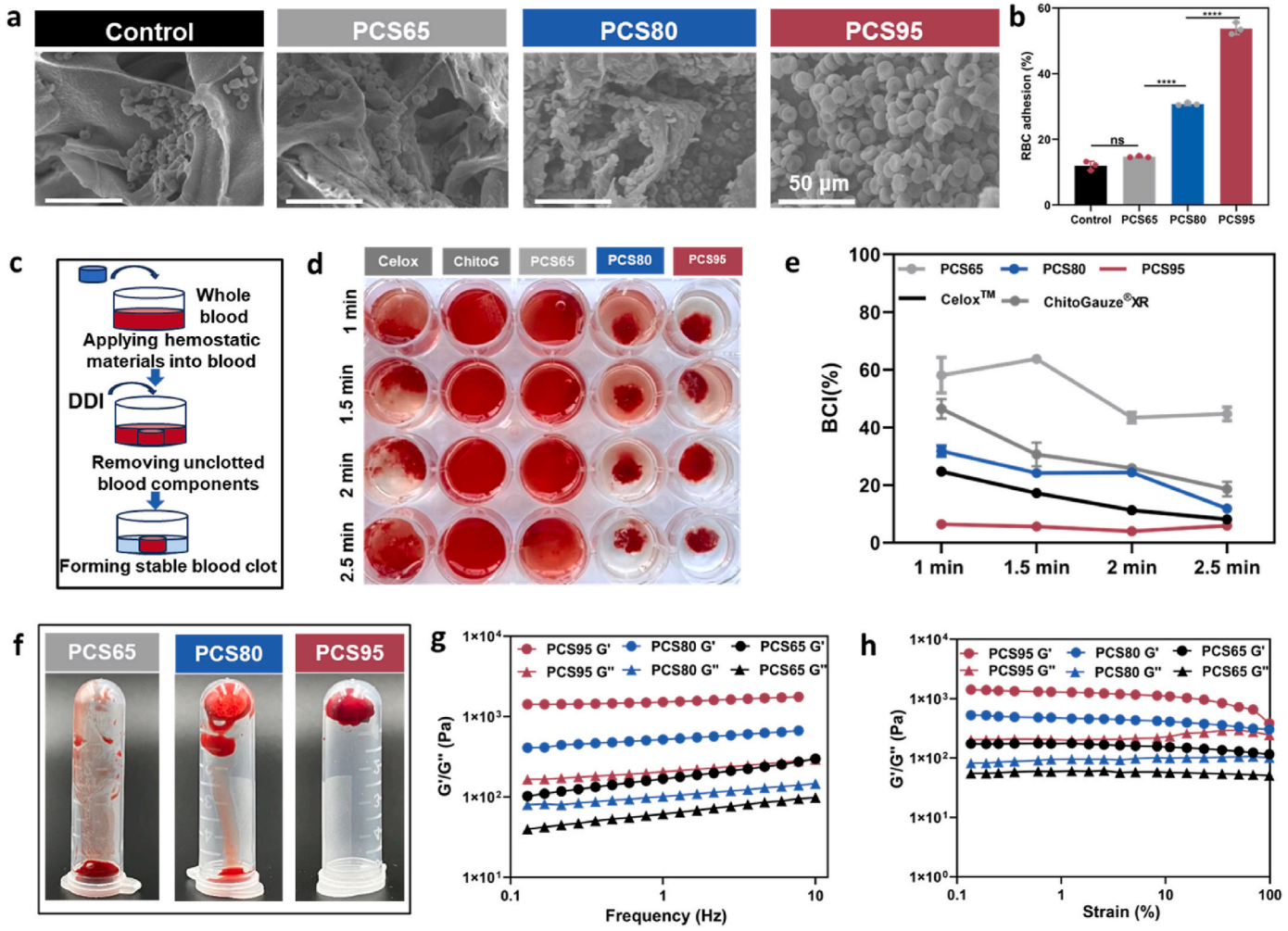

Fig. 6. Evaluation of extracorporeal hemostasis effect of PCS with different degrees of deacetylation. a) Scanning electron microscopy depicting the adhesion of red blood cells (Scale bar: 50 μm). b) Red blood cells adhesion rate of PCS (n = 3). c) Schematic illustration of hemostatic materials inducing blood clot formation *in vitro*. d) Images capturing the time-dependent behavior of blood clotting. e) Dynamic blood coagulation index (BCI) for PCS. f) Inverted tube experiment post-mixing PCS with blood, illustrating the formation of the blood clot. g) Elastic modulus (G′) and storage modulus (G″) values of the PCS sponge (indicated by red circles) after mixing with fresh blood at a frequency range from 0 to 10 Hz. h) Elastic modulus (G′) and storage modulus (G″) values of the PCS sponge (red circles) after mixing with fresh blood at a strain ranging from 0 % to 100 %. (NS, no significant differences,****P < 0.0001).

and blood maintained stability in deionized water without obvious erythrocytes rupture. The BCI value decreased with extended incubation time of blood with the materials. At a 1 min incubation, PCS95 achieved the lowest BCI value among the sample group, indicating a faster coagulation rate. After incubation for 150 s, the BCI value of PCS95 (~6 %) was significantly lower than that of PCS80, PCS65, and Celox™ and ChitoGauze®XR, indicating that PCS95 had superior hemostatic properties (Fig. 6e**)**.

As displayed in Fig. 6f**,** PCS95 effectively engaged with various active components in the blood to form a stable clot, while PCS65 had a relatively weaker effect on clot formation. Furthermore, the viscoelastic properties of blood clots formed upon contact with PCS sponges were evaluated using a rheometer. PCS95 with its strongest positive charge-carry capability, accelerated the coagulation cascade through interactions with various active blood components, including plasma proteins and blood cells. PCS95 exhibited a significantly higher storage modulus, reaching up to 1425 Pa (10 Hz) after clot formation, indicating a stronger clotting ability. In contrast, PCS80 had a lower storage modulus of 410 Pa, and PCS65 exhibited the lowest storage modulus of only 102 Pa (Fig. 6g). Additionally, the results from the rheometer in shear-strain mode were similar to those from the shear-frequency mode (Fig. 6h). These results suggested that PCS95 promoted the formation of

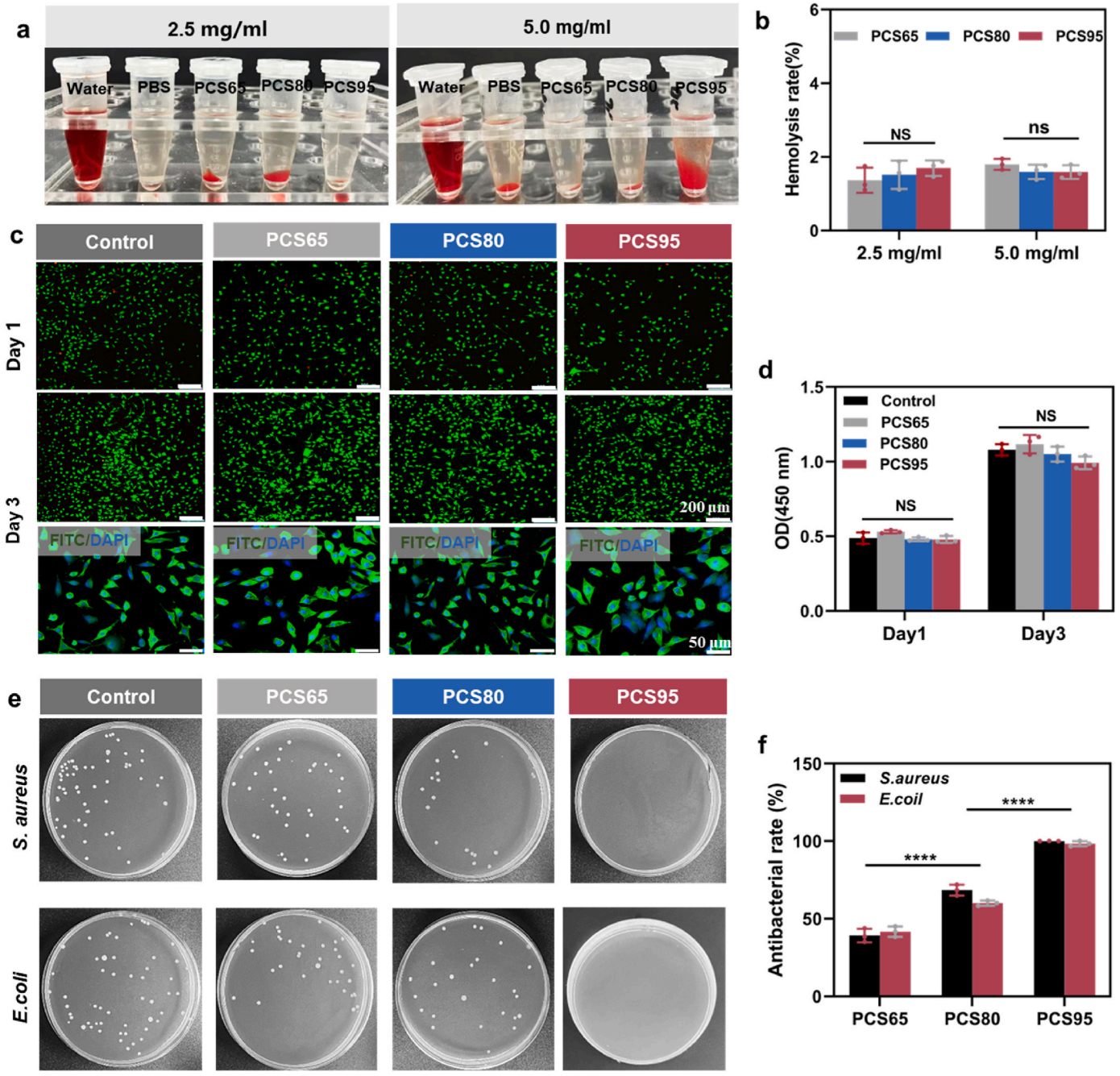

Fig. 7. Evaluation of PCS biocompatibility and antibacterial properties. a) Photographs of PCS (2.5 mg/mL, 5.0 mg/mL) incubated with blood for 1 h followed by centrifugation. b) Hemolysis rate of PCS (n = 3). c) Confocal images showing cell viability with cell Live/Dead staining (scale bar: 200 μm) and cellular morphology (scale bar: 50 μm). d) CCK-8 assay resulting for L929 cell viability (n = 3). e) Photographs demonstrating antibacterial efficacy of PCS. f) Quantification of antibacterial rate for PCS65, PCS80 and PCS95 against *Escherichia coli* (*E.Coil*) and *Staphylococcus aureus* (*S. aureus*) (n = 3). Data are expressed as the mean ± S.D. (NS, not significant, ****$p < 0.0001$).

blood clots with enhanced strength and stability relative to PCS80 and PCS65.

3.6. Biocompatibility and antibacterial of PCS

The biocompatibility of hemostatic materials is crucial for their potential clinical application. *In vitro* biocompatibility of PCS was evaluated through hemocompatibility and cell compatibility assay. Chitosan solutions at concentrations of 2.5 mg/mL and 5 mg/mL were incubated with a 5 % red blood cells (RBCs) suspension for 1 h.

As depicted in Fig. 7a, the results revealed that post-centrifugation, the supernatant from all sample groups were clear and transparent, with no significant difference from the negative control group treated with PBS. Conversely, the addition of an equal volume of Triton-X to the

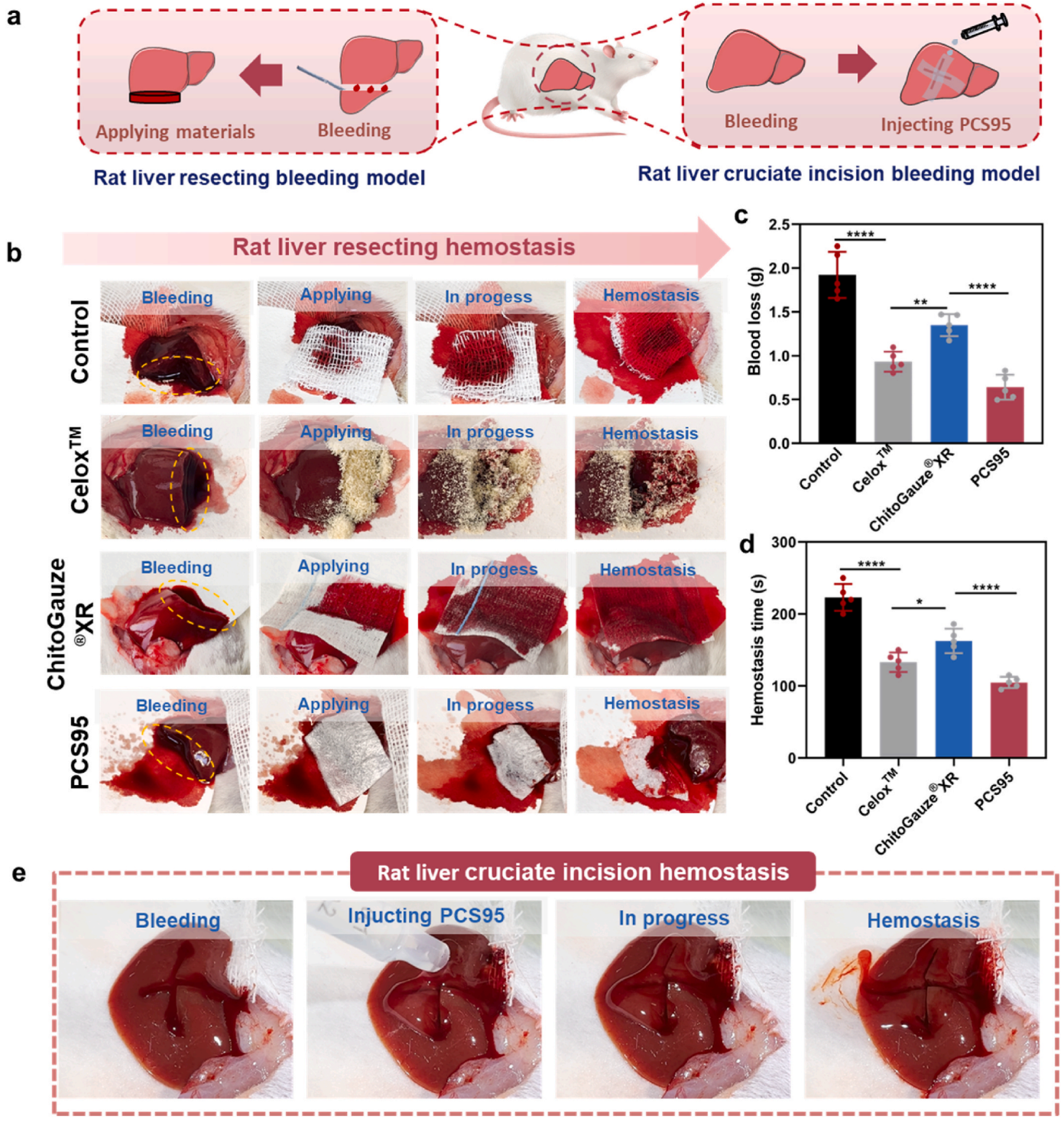

Fig. 8. Liver hemorrhage in rats. a) Schematic diagram of the hemostatic process of hemostatic agents in a rat liver resection bleeding model and rat liver incision bleeding model. b) Photographs of gauze, Celox™, Chitogauze®XR, and PCS95 during hemostasis process. c, d) Quantification of blood loss and hemostasis time for gauze, Celox™, Chitogauze®XR, and PCS95. e) Images of the hemostatic process of PCS95 solution applied to rat liver scratch wound. n = 5 rats per group. Data are expressed as mean ± SD. (NS, no significant differences, *P < 0.05, **P < 0.01, ***P < 0.001, ****P < 0.0001).

RBCs suspension induced the membrane disruptor, leading to hemoglobin release and resulting in blood-red supernatant.

The hemolysis rate in all experimental groups was below 2 % (Fig. 7b), indicating that PCS demonstrated excellent hemocompatibility. The cytotoxicity of PCS was further evaluated using L929 cells with the CCK-8 assay and live/dead staining (Fig. 7c and d). Over a 1 day and 3-day co-culture period with PCS, the cells showed robust growth, with the cell viability consistently exceeding 95 %. Additionally, PCS95 was implanted subcutaneously in SD rats for 7 and 14 days to observe its inflammatory response *in vivo*. After 7 days of PCS95 implantation, a certain level of inflammatory reaction was observed, which decreased after 14 days of implantation (Fig. S11).

In accidental bleeding accidents, wound infection is another important cause of mortality [57]. Therefore, hemostatic materials with antibacterial properties are conducive to reducing the risk of infection. The positively charged chitosan bond with the negatively charged components of bacterial cell membranes, leading to the disruption of the cell wall and consequently causing bacterial death. The antimicrobial efficacy of protonated-chitosan with different deacetylation degree against *S. aureus* and *E. coil* was tested. The growth of PCS solution on agar after co-culture with bacteria was shown in Fig. 7e. PCS molecules, carrying a positive charge, effectively destroyed bacterial cell membranes. The inhibition rate for PCS95 against *S. aureus* and *E. coli* were 99.9 ± 0.02 % and 98.3 ± 1.1 %, respectively. For PCS80, the inhibition

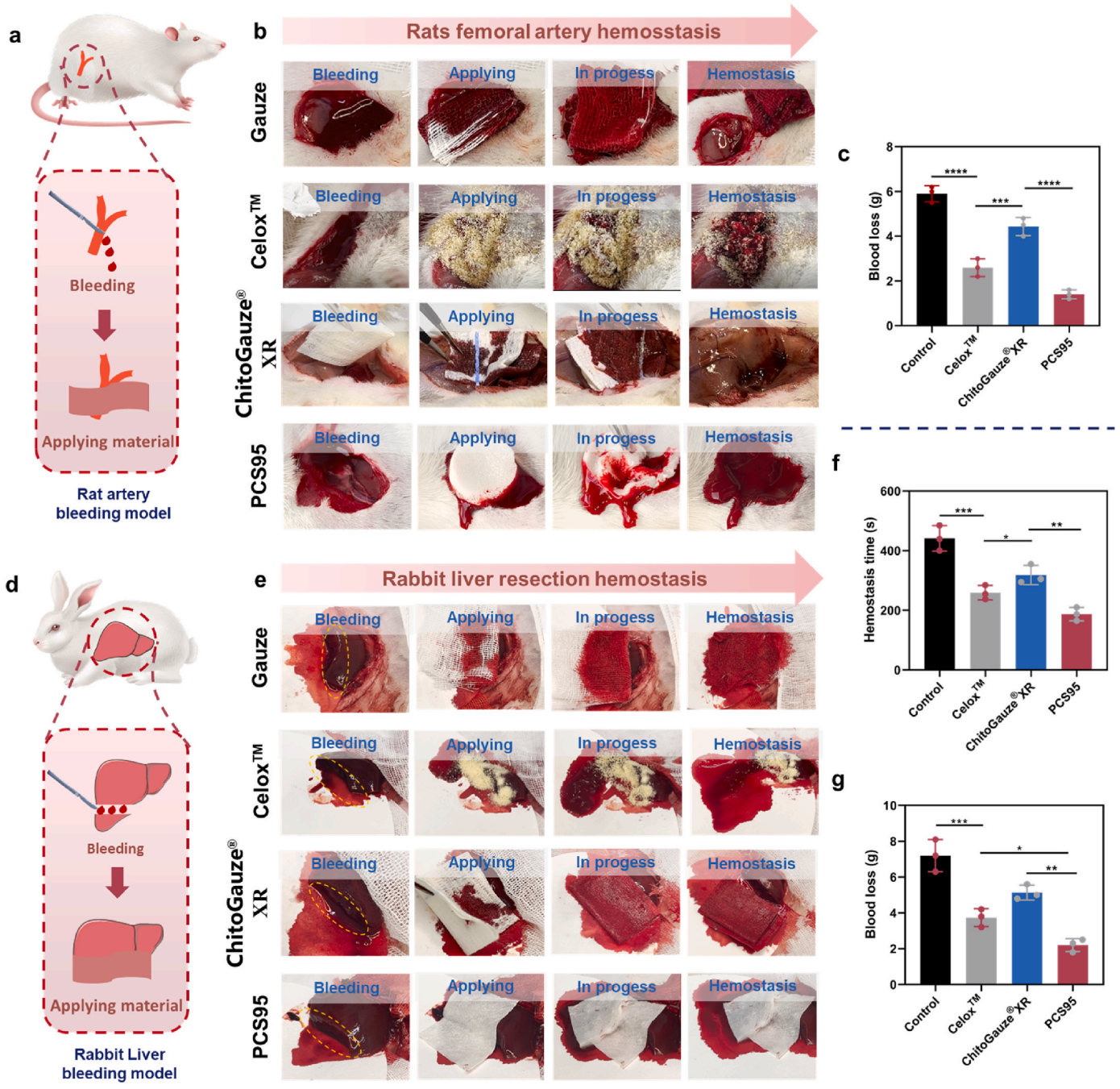

Fig. 9. Femoral artery hemorrhage in rats and liver hemorrhage in rabbits. a) Schematic diagram of femoral artery bleeding in rats. b) Photos of hemostatic material applied to the femoral artery during hemostasis in rats. c) The blood loss of femoral artery hemorrhaging rats (n = 3). d) Schematic diagram of liver bleeding in rabbit. e) Photos of hemostatic material applied to the liver during hemostasis in rabbit. f, g) Hemostasis time and blood loss of rabbit liver resection. (n = 3). Data are expressed as mean ± SD. (NS, no significant differences, *P < 0.05, **P < 0.01, ***P < 0.001, ****P < 0.0001).

rates were 68.4 ± 2.3 % for *S. aureus* and 60.0 ± 1.1 % for *E. coil*, respectively. The PCS65 showed inhibition rates of 39.1 ± 3.1 % for *S. aureus* and 41.6 ± 2.2 % for *E. coli*, respectively (Fig. 7f). In conclusion, PCS exhibited favorable good blood and cell compatibility and showed excellent superior antibacterial properties.

3.7. Hemostatic properties in vivo

In vitro hemostasis experiments revealed that PCS95 demonstrated enhanced hemostatic efficacy. Therefore, we further evaluated the hemostatic ability of PCS95 *in vivo* of PCS95 using rat models of liver resection, liver cruciate incision, and femoral artery rupture. Commercially chitosan-based hemostatic agents including ChitoGauze®XR and Celox™ were used as control groups.

Fig. 8a depicted liver resection and liver cruciate incision experiment in rats. The rat liver was excised and positioned on filter paper. Post-liver resection, hemostatic materials were applied to the wound to absorb blood. Gauze, known for high blood absorption absorbency, lacks clotting ability and merely manages blood at the wound site. ChitoGauze®XR, enriched with chitosan, features smaller fiber gaps, that effectively adsorb blood cells, forming a hemostatic barrier and minimizing blood loss.

Celox™, when applied, attracted erythrocytes to form a colloidal mass, sealing the bleeding wound (Fig. 8b). PCS95, with its NH_3^+ groups, capitalizes on the "charge" effect to promote blood coagulation by adsorbing and assembling plasma proteins in blood, activating platelets, attracting and aggregating erythrocytes. In rat liver bleeding model, PCS95 demonstrated excellent hemostasis, with a hemostasis time of 104 ± 11 s and blood loss of 0.6 ± 0.1 g (Fig. 8c and d). In contrast, gauze performed inferior hemostatic performance, with a hemostatic time of 223 ± 27 s and blood loss of 1.9 ± 0.3 g, respectively.

Bleeding in deep constricted tissues presents a challenge where the delicate bleeding site cannot be effectively managed through compression. PCS95 solution serves as a liquid hemostatic agent for non-compressible hemorrhages.

As shown in Fig. 8e, the injected PCS95 solution on the bleeding rat liver surface created a physical barrier, significantly reducing wound bleeding (Mov. S2).

A rat femoral artery bleeding model was employed to assess the material's hemostatic ability in a larger bleeding wound (Fig. 9a). Femoral artery hemorrhage is characterized by rapid blood flow and large amount of blood loss, with a high fatality rate. Due to the extensive bleeding in rats, material removal for hemostasis confirmation was impractical, so the blood loss was measured to judge the material's hemostasis efficacy. Gauze's absorbency was insufficient for hemostasis, requiring manual compression to stop bleeding. In contrast, Celox™ powder did not rapidly absorb the blood. Instead, it formed a physical barrier that progressively transformed into a gel obstruct blood flow. ChitosGauze®XR a composite of chitosan and gauze, had a stiffer texture that did not conform adequately to the bleeding site, with a slightly inferior hemostatic efficacy than Celox™, yielding an approximate blood loss of 4.4 g PCS95 sponge, when filled into the bleeding area, interacted with blood components to promote blood coagulation (Fig. 9b). With its a soft texture, could be adequately filled into the wound and make full contact with the bleeding site. It accelerated the coagulation process by concentrating active blood components and leveraging the charge effect of the $–NH_3^+$ groups. Compared to others group, PCS95 effectively controlled bleeding within 2 g (Fig. 9c), significantly reducing blood loss.

As population ages, the incidence of conditions such as atrial fibrillation and cardiovascular diseases has seen a significant increase. It is often necessary to use anticoagulant drugs (such as warfarin, aspirin, etc.) prevent thrombosis in these patient populations.

However, the use of these anticoagulants is associated with an increased risk of bleeding-related mortality, posing a greater challenge for the development of novel hemostatic materials [58]. Our investigation has revealed that the amino groups ($-NH_3^+$) on protonated-chitosan molecules interact with active components in the blood (such as plasma proteins, platelets, erythrocytes, etc.) to promote coagulation. Additionally, recent studies have found that chitosan activates Toll-like receptor 2 (TLR2) on platelets, a receptor not currently inhibited by existing anticoagulants (eptifibatide, clopidogrel, aspirin, etc.). This allows chitosan to initiate the coagulation cascade even in an anticoagulant-enriched environment [2]. To assess the hemostatic efficacy of PCS95, we constructed a rabbit model with an induced coagulation disorder and oral anticoagulant aspirin. A liver incision (1.0 cm in width) was created as the rabbit liver bleeding model (Fig. 9d). Aspirin inhibits platelet aggregation by irreversibly inhibiting the enzyme cyclooxygenase (COX) and blocking the synthesis of thromboxane A2 (TXA2) [59]. Gauze had minimal procoagulant properties and primarily controlled bleeding through blood absorption. Its hemostasis time exceeded 8 min, with a blood loss exceeding 7.5 g. Although Celox™ and Chitogauze®XR both containing chitosan as their main ingredient, their molecular charge density was lower than that of PCS95, resulting in weaker hemostatic performance compared to PCS95 (Fig. 9e). PCS95 operated a multi-channel hemostatic mechanism, creating a pro-coagulation environment on the wound surface (Mov. S3), and effectively controlling bleeding within 3 min and with a blood loss of only 2.2 g (Fig. 9f and g).

Overall, PCS95 enhanced blood clotting by facilitating the assembly plasma proteins, engaging coagulation factors, stimulating platelets activation, and adhering to erythrocytes. Compared to non-protonated hemostatic products such as Celox™ and ChitoGauze®XR, PCS95 exhibited superior hemostatic effects *in vivo*.

4. Discussion

The issue of life loss due to severe bleeding has long been a profound concern, especially the elderly population, who often takes anticoagulants, leading to asignificant increased risk of uncontrollable hemorrhages [60]. This challenge calls for the development of innovative hemostatic materials to address complex bleeding scenarios.

Chitosan, with its positively charged molecular structure, has shown notable hemostatic efficacy by aggregating erythrocytes and platelets, even in coagulopathy cases, thus widely used as active hemostatic agent [61,62]. However, previous studies mainly focused on the chemical modification and functional application of chitosan molecules, and few studies focused on the underlying hemostasis mechanism of chitosan molecules. We assume that a deep understanding of the interaction between materials and blood at the molecular level is crucial for designing new chitosan-based hemostatic agents.

In most studies, the $–NH_2$ groups have often been excessively consumed as cross-linking sites during material formation, which undoubtedly compromises the coagulation properties of chitosan [28, 63–65]. Interesting, we have discovered that once the amount of $–NH_3^+$ groups on chitosan molecular chains exceeded a certain threshold (>4.9 mmol/g), the coagulation-promoting effect undergone a qualitative transformation.

Our research highlights the pivotal role of the $–NH_3^+$ group on the chitosan molecular chains in promoting coagulation, an aspect that has not been adequately recognized in the literature. In this study, we discovered the interface phenomenon where PCS formed protein membrane upon introduction into plasma. The conditions necessary for this phenomenon to occur and the interactions between PCS and plasma proteins, RBCs, and platelets were investigated. The results indicated that protonation of chitosan enabled the in-situ recruitment of coagulation proteins presented in plasma, such as FII, FV, FIX and FXII. PCS activated platelets, which in turn secreted various coagulation-related factors including FXI, FX, FV, PF4, ADP, 5-TH and so on. The activated platelets facilitate the assembly and reaction of these coagulation factors, enhancing the activity of the active site and accelerating the generation of the coagulation cascade, ultimately promoting the bigger

blood clot formation. To explain the coagulation mechanism of PCS, a "three-stage rocket" model was proposed. This model was further extended to chitosan-based derivatives (Figs. S12–14), including Quaternized-chitosan (QCS), Catechol-chitosan (CHI–C), and Alkylated-chitosan (ACS). For all three chitosan derivatives, the addition to PPP solution resulted in the formation of protein membranes, and promoted the generation of protein clots in PRP solution (Fig. S15).

Additionally, natural polysaccharide materials such as gelatin, cellulose, and dextran are commonly used as hemostatic agents. Gelatin promotes hemostasis by activating platelets and concentrating the blood [66]. Cellulose aids in hemostasis by concentrating blood, activating coagulation factors, and promoting platelet aggregation [8,67]. Dextran facilitates hemostasis by enhancing platelet adhesion, although it lacks the ability to activate platelets [68]. Due to the unique positive charge effects of chitosan molecules, they interact with various active components in the blood to promote coagulation, thereby showing superior coagulation-enhancing effects. However, both chitosan and cellulose degrade slowly in the body, and their long-term use as internal hemostats should be carefully considered. Utilizing protonated-chitosan molecules as molecular templates enables the integrated construction of hemostatic materials with procoagulant properties, providing a reliable foundation for the design of next-generation materials aimed at hemostasis in coagulation disorders.

5. Conclusion

In summary, we initially discovered the phenomenon of protein membrane formation through the interaction between protonated-chitosan and plasma proteins. We investigated the conditions necessary for the formation of these protein membranes, analyzed the protein composition within the membranes via proteomics, and studied the binding process between protonated chitosan and plasma proteins using isothermal titration calorimetry and molecular dynamics simulations. We confirmed that the $-NH_3^+$ groups on molecular chains of protonated-chitosan were the critical functional groups for promoting coagulation. PCS accelerated the coagulation cascade by recruiting clotting factors and assembling plasma proteins, activating platelets, and enhancing the secretion of clotting substances by platelets. PCS exhibited excellent biocompatibility and antibacterial properties *in vitro*. Furthermore, in hemostatic experiments conducted both *in vitro* and *vivo*, such as tests on rabbit liver resections with compromised platelet functionality due to aspirin, PCS95 sponges demonstrated superior efficacy compared to commercial chitosan-based hemostatic products like Celox™ and ChitoGauze®XR.

Ethics approval and consent to participate

All experimental procedures adhered to the relevant ethical guidelines, and the use of animals in this study was approved by animal Ethics Committee, East China University of Science and Technology. The ethical approval Number was *ECUST-21046*.

CRediT authorship contribution statement

Zhenhua Huang: Writing – original draft, Data curation, Conceptualization. **Dong Zhang:** Visualization, Software, Conceptualization. **Laiqiang Tong:** Writing – review & editing, Visualization, Investigation. **Fan Gao:** Methodology, Formal analysis. **Shaozang Zhang:** Supervision, Formal analysis. **Xinqing Wang:** Software, Resources, Formal analysis. **Yina Xie:** Visualization. **Fangping Chen:** Writing – review & editing, Resources, Project administration, Conceptualization. **Changsheng Liu:** Resources, Project administration, Conceptualization.

Declaration of competing interest

There are no conflicts to declare.

Acknowledgements

This investigation was supported by the National Natural Science Foundation of China (No. 32171342 ; 51772100), National Key Research and Development Program of China (2022YFB3804300). The authors thank Research Center of Analysis and Test of East China University of Science and Technology for the help on the characterization.

Appendix A. Supplementary data

Supplementary data to this article can be found online at https://doi.org/10.1016/j.bioactmat.2024.07.012.

References

[1] H. Yuk, J. Wu, T.L. Sarrafian, X. Mao, C.E. Varela, E.T. Roche, L.G. Griffiths, C. S. Nabzdyk, X. Zhao, Rapid and coagulation-independent haemostatic sealing by a paste inspired by barnacle glue, Nat. Biomed. Eng. 5 (10) (2021) 1131–1142.
[2] V.K. Lee, T. Lee, A. Ghosh, T. Saha, M.V. Bais, K.K. Bharani, M. Chag, K. Parikh, P. Bhatt, B. Namgung, G. Venkataramanan, A. Agrawal, K. Sonaje, L. Mavely, S. Sengupta, R.A. Mashelkar, H.L. Jang, An architecturally rational hemostat for rapid stopping of massive bleeding on anticoagulation therapy, Proc. Natl. Acad. Sci. USA 121 (5) (2024) e2316170121.
[3] K. Kim, J.H. Ryu, M.-Y. Koh, S.P. Yun, S. Kim, J.P. Park, C.-W. Jung, M.S. Lee, H.-I. Seo, J.H. Kim, H. Lee, Coagulopathy-independent, bioinspired hemostatic materials: a full research story from preclinical models to a human clinical trial, Sci. Adv. 7 (13) (2021) eabc9992.
[4] Y. Guo, Y. Wang, X. Zhao, X. Li, Q. Wang, W. Zhong, K. Mequanint, R. Zhan, M. Xing, G. Luo, Snake extract–laden hemostatic bioadhesive gel cross-linked by visible light, Sci. Adv. 7 (29) (2021) eabf9635.
[5] Q. Li, E. Hu, K. Yu, R. Xie, F. Lu, B. Lu, R. Bao, T. Zhao, F. Dai, G. Lan, Self-propelling janus particles for hemostasis in perforating and irregular wounds with massive hemorrhage, Adv. Funct. Mater. 30 (42) (2020) 2004153.
[6] Q. Yu, B. Su, W. Zhao, C. Zhao, Janus self-propelled chitosan-based hydrogel spheres for rapid bleeding control, Adv. Sci. 10 (5) (2023) 2205989.
[7] J.R. Baylis, J.H. Yeon, M.H. Thomson, A. Kazerooni, X. Wang, A.E. St John, E. B. Lim, D. Chien, A. Lee, J.Q. Zhang, J.M. Piret, L.S. Machan, T.F. Burke, N. J. White, C.J. Kastrup, Self-propelled particles that transport cargo through flowing blood and halt hemorrhage, Sci. Adv. 1 (9) (2015) e1500379.
[8] L. Bao, Z. Zhang, X. Li, L. Zhang, H. Tian, M. Zhao, T. Ye, W. Cui, Bacteriosynthetic degradable tranexamic acid-functionalized short fibers for inhibiting invisible hemorrhage, Small 19 (47) (2023) 2303615.
[9] J. Chen, Z. Huang, H. Zhang, Z. Zhang, D. Wang, D. Xia, C. Yang, M. Dong, Three-dimensional layered nanofiber sponge with in situ grown silver- metal organic framework for enhancing wound healing, Chem. Eng. J. 443 (2022) 136234.
[10] J. Lee, E. Kim, K.-J. Kim, J.W. Rhie, K.I. Joo, H.J. Cha, Protective topical dual-sided nanofibrous hemostatic dressing using mussel and silk proteins with multifunctionality of hemostasis and anti-bacterial infiltration, Small 20 (18) (2024) 2308833.
[11] X. Zhang, X. Wang, P. Yuan, C. Ma, Y. Wang, Z. Zhang, P. Wang, Y. Zhao, W. Wu, A 3d-printed cuttlefish bone elastomeric sponge rapidly controlling noncompressible hemorrhage, Small 20 (19) (2024) 2307041.
[12] M. Li, G. Pan, Y. Yang, B. Guo, Smart aligned multi-layered conductive cryogels with hemostasis and breathability for coagulopathy epistaxis, nasal mucosal repair and bleeding monitoring, Nano Today 48 (2023) 101720.
[13] X. Zhao, B. Guo, H. Wu, Y. Liang, P.X. Ma, Injectable antibacterial conductive nanocomposite cryogels with rapid shape recovery for noncompressible hemorrhage and wound healing, Nat. Commun. 9 (1) (2018) 2784.
[14] E.E. Leonhardt, N. Kang, M.A. Hamad, K.L. Wooley, M. Elsabahy, Absorbable hemostatic hydrogels comprising composites of sacrificial templates and honeycomb-like nanofibrous mats of chitosan, Nat. Commun. 10 (1) (2019) 2307.
[15] X. Du, L. Wu, H. Yan, Z. Jiang, S. Li, W. Li, Y. Bai, H. Wang, Z. Cheng, D. Kong, L. Wang, M. Zhu, Microchannelled alkylated chitosan sponge to treat noncompressible hemorrhages and facilitate wound healing, Nat. Commun. 12 (1) (2021) 4733.
[16] L. Qi, L. Mu, X. Guo, A. Liu, C. Chen, Q. Ye, Z. Zhong, X. Shi, Fast expandable chitosan-fibers cryogel from ambient drying for noncompressible bleeding control and in situ tissue regeneration, Adv. Funct. Mater. 33 (16) (2023) 2212231.
[17] H. Zhu, T. Yang, S. Chen, X. Wang, J. He, Y. Luo, Construction and characterization of chitosan/poly(acrylamide-[2-(methacryloyloxy)ethyl]trimethylammonium chloride) double-network hydrogel with enhanced antibacterial activity, Adv. Compos. Hybrid Mater. 6 (6) (2023) 192.
[18] S. Meng, H. Hu, Y. Qiao, F. Wang, B.N. Zhang, D. Sun, L. Zhou, L. Zhao, L. Xie, H. Zhang, Q. Zhou, A versatile hydrogel with antibacterial and sequential drug-releasing capability for the programmable healing of infectious keratitis, ACS Nano 17 (23) (2023) 24055–24069.
[19] Y. Feng, H.-L. Gao, D. Wu, Y.-T. Weng, Z.-Y. Wang, S.-H. Yu, Z. Wang, Biomimetic lamellar chitosan scaffold for soft gingival tissue regeneration, Adv. Funct. Mater. 31 (43) (2021) 2105348.
[20] F.-C. Chang, M.M. James, A.M. Qassab, Y. Zhou, Y. Ando, M. Shi, M. Zhang, 3d chitosan scaffolds support expansion of human neural stem cells in chemically defined condition, Matter 6 (10) (2023) 3631–3660.

[21] L. Xiao, P. Xie, J. Ma, K. Shi, Y. Dai, M. Pang, J. Luo, Z. Tan, Y. Ma, X. Wang, L. Rong, L. He, A bioinspired injectable, adhesive, and self-healing hydrogel with dual hybrid network for neural regeneration after spinal cord injury, Adv. Mater. 35 (41) (2023) 2304896.
[22] Y. Wang, J. Guo, X. Cao, Y. Zhao, Developing conductive hydrogels for biomedical applications, Smart Medicine 3 (1) (2024) e20230023.
[23] S. Yang, F. Wang, H. Han, H.A. Santos, Y. Zhang, H. Zhang, J. Wei, Z. Cai, Fabricated technology of biomedical micro-nano hydrogel, Biomedical Technology 2 (2023) 31–48.
[24] M.D. William G. Malette, J. Herbert, M.D. Quigley, D. Ray, M.D. Gaines, D. Norris, M.D. Johnson, W. Gerald Rainer M.D, Chitosan: a new hemostatic, Ann. Thorac. Surg. 36 (1983) 55–58.
[25] B. Guo, R. Dong, Y. Liang, M. Li, Haemostatic materials for wound healing applications, Nat. Rev. Chem 5 (11) (2021) 773–791.
[26] G. Gan, X. Xu, X. Chen, X.F. Zhang, J. Wang, C.Q. Zhong, Scasp: a simple and robust sds-aided sample preparation method for proteomic research, Mol. Cell. Proteomics : MCP 20 (2021) 100051.
[27] L. Zheng, Q. Wang, Y.S. Zhang, H. Zhang, Y. Tang, Y. Zhang, W. Zhang, X. Zhang, A hemostatic sponge derived from skin secretion of andrias davidianus and nanocellulose, Chem. Eng. J. 416 (2021) 129136.
[28] K. Zhang, Y. Xian, M. Li, Z. Pan, Z. Zhu, Y. Yang, H. Wang, L. Zhang, C. Zhang, D. Wu, Gelable and adhesive powder for lethal non-compressible hemorrhage control, Adv. Funct. Mater. 33 (46) (2023) 2305222.
[29] J. Yang, F. Tian, Z. Wang, Q. Wang, Y.-J. Zeng, S.-Q. Chen, Effect of chitosan molecular weight and deacetylation degree on hemostasis, J. Biomed. Mater. Res. B Appl. Biomater. 84B (1) (2008) 131–137.
[30] S. Sreekumar, J. Wattjes, A. Niehues, T. Mengoni, A.C. Mendes, E.R. Morris, F. M. Goycoolea, B.M. Moerschbacher, Biotechnologically produced chitosans with nonrandom acetylation patterns differ from conventional chitosans in properties and activities, Nat. Commun. 13 (1) (2022) 7125.
[31] Q. Xu, E. Hu, H. Qiu, L. Liu, Q. Li, B. Lu, K. Yu, F. Lu, R. Xie, G. Lan, Y. Zhang, Catechol-chitosan/carboxymethylated cotton-based janus hemostatic patch for rapid hemostasis in coagulopathy, Carbohydr. Polym. 315 (2023) 120967.
[32] Y. Zhang, J.L.Y. Wu, J. Lazarovits, W.C.W. Chan, An analysis of the binding function and structural organization of the protein corona, J. Am. Chem. Soc. 142 (19) (2020) 8827–8836.
[33] C.A. LeDuc, L. Vroman, E.F. Leonard, A mathematical model for the vroman effect, Ind. Eng. Chem. Res. 34 (10) (1995) 3488–3495.
[34] R. Madathiparambil Visalakshan, L.E. Gonzalez Garcia, M.R. Benzigar, A. Ghazaryan, J. Simon, A. Mierczynska-Vasilev, T.D. Michl, A. Vinu, V. Mailander, S. Morsbach, K. Landfester, K. Vasilev, The influence of nanoparticle shape on protein corona formation, Small 16 (25) (2020) e2000285.
[35] J. Ren, N. Andrikopoulos, K. Velonia, H. Tang, R. Cai, F. Ding, P.C. Ke, C. Chen, Chemical and biophysical signatures of the protein corona in nanomedicine, J. Am. Chem. Soc. 144 (21) (2022) 9184–9205.
[36] X. Chen, J. Chen, N. Huang, The structure, formation, and effect of plasma protein layer on the blood contact materials: a review, Biosurf. Biotribol. 8 (1) (2022) 1–14.
[37] H. Yan, H. Yang, A. Li, R. Cheng, Ph-tunable surface charge of chitosan/graphene oxide composite adsorbent for efficient removal of multiple pollutants from water, Chem. Eng. J. 284 (2016) 1397–1405.
[38] B.M. Mohammed, A. Matafonov, I. Ivanov, M.-f. Sun, Q. Cheng, S.K. Dickeson, C. Li, D. Sun, I.M. Verhamme, J. Emsley, D. Gailani, An update on factor xi structure and function, Thromb. Res. 161 (2018) 94–105.
[39] M.I. Hassan, A. Saxena, F. Ahmad, Structure and function of von willebrand factor, Blood Coagul. Fibrinolysis 23 (1) (2012) 11–22.
[40] M. Pathak, P. Wilmann, J. Awford, C. Li, B.K. Hamad, P.M. Fischer, I. Dreveny, L. V. Dekker, J. Emsley, Coagulation factor xii protease domain crystal structure, J. Thromb. Haemostasis 13 (4) (2015) 580–591.
[41] Y. Qiu, A.C. Brown, D.R. Myers, Y. Sakurai, R.G. Mannino, R. Tran, B. Ahn, E. T. Hardy, M.F. Kee, S. Kumar, G. Bao, T.H. Barker, W.A. Lam, Platelet mechanosensing of substrate stiffness during clot formation mediates adhesion, spreading, and activation, Proc. Natl. Acad. Sci. USA 111 (40) (2014) 14430–14435.
[42] Isothermal titration calorimetry, Nat. Rev. Meth. Primers 3 (1) (2023) 18.
[43] J.-Y. Park, S.J. Park, J.Y. Park, S.-H. Kim, S. Kwon, Y. Jung, D. Khang, Unfolded protein corona surrounding nanotubes influence the innate and adaptive immune system, Adv. Sci. 8 (8) (2021) 2004979.
[44] K. Suzuki-Inoue, Platelets and cancer-associated thrombosis: Focusing on the platelet activation receptor clec-2 and podoplanin, Blood 134 (22) (2019) 1912–1918.
[45] K.E. Hally, A.C. La Flamme, P.D. Larsen, S.A. Harding, Platelet toll-like receptor (tlr) expression and tlr-mediated platelet activation in acute myocardial infarction, Thromb. Res. 158 (2017) 8–15.
[46] P.E.J. van der Meijden, J.W.M. Heemskerk, Platelet biology and functions: new concepts and clinical perspectives, Nat. Rev. Cardiol. 16 (3) (2019) 166–179.
[47] S.A. Smith, The cell-based model of coagulation, J. Vet. Emerg. Crit. Care 19 (1) (2009) 3–10.
[48] F. Swieringa, H.M.H. Spronk, J.W.M. Heemskerk, P.E.J. van der Meijden, Integrating platelet and coagulation activation in fibrin clot formation, Res. Pract. Thrombosis Haemostasis 2 (3) (2018) 450–460.
[49] N. Abbasian, S.L. Millington-Burgess, S. Chabra, J.-D. Malcor, M.T. Harper, Supramaximal calcium signaling triggers procoagulant platelet formation, Blood Adv. 4 (1) (2020) 154–164.
[50] P. Blair, R. Flaumenhaft, Platelet α-granules: basic biology and clinical correlates, Blood Rev. 23 (4) (2009) 177–189.
[51] M.S. Lord, B. Cheng, B.L. Farrugia, S. McCarthy, J.M. Whitelock, Platelet factor 4 binds to vascular proteoglycans and controls both growth factor activities and platelet activation, J. Biol. Chem. 292 (10) (2017) 4054–4063.
[52] B. Estevez, X. Du, New concepts and mechanisms of platelet activation signaling, Physiology 32 (2) (2017) 162–177.
[53] M.H. Periayah, A.S. Halim, A.Z. Mat Saad, Mechanism action of platelets and crucial blood coagulation pathways in hemostasis, Int. J. Hematol. Oncol. Stem Cell Res. 11 (4) (2017) 319–327.
[54] M. Tomaiuolo, L.F. Brass, T.J. Stalker, Regulation of platelet activation and coagulation and its role in vascular injury and arterial thrombosis, Intervent. Cardiol. Clinics 6 (1) (2017) 1–12.
[55] X. Shang, H. Chen, V. Castagnola, K. Liu, L. Boselli, V. Petseva, L. Yu, L. Xiao, M. He, F. Wang, K.A. Dawson, J. Fan, Unusual zymogen activation patterns in the protein corona of ca-zeolites, Nat. Catal. 4 (7) (2021) 607–614.
[56] J.W. Weisel, R.I. Litvinov, Red blood cells: the forgotten player in hemostasis and thrombosis, J. Thromb. Haemostasis 17 (2) (2019) 271–282.
[57] Z. Luo, J. Che, L. Sun, L. Yang, Y. Zu, H. Wang, Y. Zhao, Microfluidic electrospray photo-crosslinkable κ-carrageenan microparticles for wound healing, Eng. Regenerat. 2 (2021) 257–262.
[58] J.K. Schaefer, J. Errickson, X. Gu, T. Alexandris-Souphis, M.A. Ali, B. Haymart, S. Kaatz, E. Kline-Rogers, J.H. Kozlowski, G.D. Krol, V. Shah, S.L. Sood, J. B. Froehlich, G.D. Barnes, Assessment of an intervention to reduce aspirin prescribing for patients receiving warfarin for anticoagulation, JAMA Netw. Open 5 (9) (2022) e2231973.
[59] V. Bertelé, A. Falanga, M. Tomasiak, E. Dejana, C. Cerletti, G. de Gaetano, Platelet thromboxane synthetase inhibitors with low doses of aspirin: possible resolution of the "aspirin dilemma", Science 220 (4596) (1983) 517–519.
[60] I. Anderson, A.S. Cifu, Management of bleeding in patients taking oral anticoagulants, JAMA 319 (19) (2018) 2032–2033.
[61] B. Hu, G. Bao, X. Xu, K. Yang, Topical hemostatic materials for coagulopathy, J. Mater. Chem. B 10 (12) (2022) 1946–1959.
[62] X. Zhao, Y. Liang, B. Guo, Z. Yin, D. Zhu, Y. Han, Injectable dry cryogels with excellent blood-sucking expansion and blood clotting to cease hemorrhage for lethal deep-wounds, coagulopathy and tissue regeneration, Chem. Eng. J. 403 (2021) 126329.
[63] Y. Zhang, Y. Wang, L. Chen, J. Zheng, X. Fan, X. Xu, G. Zhou, N. Ullah, X. Feng, An injectable antibacterial chitosan-based cryogel with high absorbency and rapid shape recovery for noncompressible hemorrhage and wound healing, Biomaterials 285 (2022) 121546.
[64] B. Lu, E. Hu, W. Ding, W. Wang, R. Xie, K. Yu, F. Lu, G. Lan, F. Dai, Bioinspired hemostatic strategy via pulse ejections for severe bleeding wounds, Research 6 (2023) 150.
[65] X. Zhao, Y. Huang, Z. Li, J. Chen, J. Luo, L. Bai, H. Huang, E. Cao, Z. Yin, Y. Han, B. Guo, Injectable self-expanding/self-propelling hydrogel adhesive with procoagulant activity and rapid gelation for lethal massive hemorrhage management, Adv. Mater. (2024) 2308701.
[66] X. Xie, D. Li, Y. Chen, Y. Shen, F. Yu, W. Wang, Z. Yuan, Y. Morsi, J. Wu, X. Mo, Conjugate electrospun 3d gelatin nanofiber sponge for rapid hemostasis, Adv. Healthcare Mater. 10 (20) (2021) 2100918.
[67] H. He, W. Zhou, J. Gao, F. Wang, S. Wang, Y. Fang, Y. Gao, W. Chen, W. Zhang, Y. Weng, Z. Wang, H. Liu, Efficient, biosafe and tissue adhesive hemostatic cotton gauze with controlled balance of hydrophilicity and hydrophobicity, Nat. Commun. 13 (1) (2022) 552.
[68] C. Liu, X. Liu, C. Liu, N. Wang, H. Chen, W. Yao, G. Sun, Q. Song, W. Qiao, A highly efficient, in situ wet-adhesive dextran derivative sponge for rapid hemostasis, Biomaterials 205 (2019) 23–37.